



Published in final edited form as:

Nature. 2020 October ; 586(7831): 730–734. doi:10.1038/s41586-020-2728-4.

Stimulus-specific hypothalamic encoding of a persistent defensive state

Ann Kennedy^{1,*}, Prabhat S. Kunwar^{1,*†}, Ling-yun Li^{1,*}, Stefanos Stagkourakis¹, Daniel A. Wagenaar¹, David J. Anderson^{1,2,3}

¹Division of Biology and Biological Engineering 156-29, Tianqiao and Chrissy Chen Institute for Neuroscience, California Institute of Technology, Pasadena, California 91125, USA

²Howard Hughes Medical Institute, California Institute of Technology, 1200 East California Blvd, Pasadena, California 91125 USA

Summary

Persistent neural activity has been described in cortical, hippocampal, and motor networks as mediating working memory of transiently encountered stimuli^{1,2}. Internal emotion states such as fear also exhibit persistence following exposure to an inciting stimulus³, but whether slow neural dynamics are involved is not well-studied. SF1⁺/Nr5a1⁺ neurons in the dorsomedial and central subdivisions of the ventromedial hypothalamus (VMHdm/c) are necessary for defensive responses to predators^{4–7}. Optogenetic activation of VMHdm^{SF1} neurons elicits defensive behaviours that outlast stimulation^{5,8}, suggesting the induction of a persistent internal state of fear or anxiety. Here we show that in response to naturalistic threatening stimuli, VMHdm^{SF1} neurons exhibit persistent activity lasting many tens of seconds. This persistent activity was correlated with, and required for, persistent defensive behavior in an open-field assay, and was dependent on neurotransmitter release from VMHdm^{SF1} neurons. Stimulation and calcium imaging experiments in acute slices revealed local excitatory connectivity between VMHdm^{SF1} neurons. Microendoscopic calcium imaging of VMHdm^{SF1} neurons revealed that persistent activity at the population level reflects heterogeneous dynamics among individual cells. Unexpectedly, distinct but overlapping VMHdm^{SF1} subpopulations were persistently activated by different modalities of threatening stimuli. Computational modeling suggests that neither recurrent excitation nor slow-acting neuromodulators alone can account for persistent activity that maintains stimulus identity. Our results identify stimulus-specific slow neural dynamics in the hypothalamus, on a time scale orders

Users may view, print, copy, and download text and data-mine the content in such documents, for the purposes of academic research, subject always to the full Conditions of use:http://www.nature.com/authors/editorial_policies/license.html#terms

³Author for correspondence (wuwei@caltech.edu).

[†]Present address: Kallyope, Inc. 430 E 29th St, New York, NY 10016 USA

*These authors contributed equally to this work.

AUTHOR CONTRIBUTIONS

AK, PK, and DJA conceptualized and designed the fiber photometry and microendoscopic imaging experiments. AK, LL, PK, and DJA conceptualized and designed the optogenetic loss-of-function experiments. DAW and PK designed and built the imaging acquisition setup. PK performed imaging experiments. LL performed loss-of-function, rat exposure assay + imaging, tetanus toxin, and extracellular recording experiments. SS performed slice electrophysiology experiments. AK performed imaging data analysis and modeling. AK, PK, LL, and DJA wrote the manuscript.

COMPETING INTERESTS

The authors declare no competing interests.

of magnitude longer than that supporting working memory in the cortex^{9,10}, as a contributing mechanism underlying a persistent emotion state. (238 words)

We performed fiber photometry¹¹ in VMHdm^{SF1} neurons expressing GCaMP6s in freely behaving mice in their home cage, during a 10s presentation of a predator (an anesthetized rat¹²) (Fig. 1a–c). We observed a rapid increase in signal at the onset of rat presentation (Fig. 1d, e). Remarkably, this activity persisted for over a minute following rat removal (time constant $\tau_{\text{decay}} = 26.7 \pm 2.2$ seconds; Fig. 1d–e). In contrast, a toy rat evoked a weaker and shorter response (Fig. 1d, e). Peak responses to multiple presentations of the rat decreased over trials and days, suggesting habituation (ED Fig. 7).

To better control stimulus presentation, we repeated this experiment using a head-fixed preparation, with stimuli enclosed in a wire cage to prevent contact. VMHdm^{SF1} peak responses varied by stimuli, with rat responses being strongest and longest-lasting (Fig. 1f–h; ED Fig. 1). VMHdm^{SF1} persistent activity is unlikely to reflect slow GCaMP6s decay kinetics (Fig. 2 and ED Fig. 6). As expected¹², VMHdm^{SF1} neurons responded moderately to rat urine, and weakly to an overhead looming disk (ED Fig. 1); defensive responses to the latter¹³ do not require VMHdm^{SF1} neurons⁵.

To better measure and correlate defensive behaviours in freely moving animals with VMHdm^{SF1} neuronal activity, we devised a novel rat exposure assay in an open field arena. A mouse was introduced to the arena, and after ten minutes of habituation an awake rat in a cage was presented above the arena for 15 seconds. Following rat exposure, mice exhibited thigmotaxis, an index of increased anxiety¹⁴, lasting minutes (Fig. 1k; Fig. 1l–n, **blue curves**). Freezing, jumping and a transient decrease in velocity were observed in some animals, but were not significantly different from controls. Thigmotaxis was not observed if the mouse was introduced after rat presentation, arguing that lingering rat-derived odors are not causative (ED Fig. 2a–c). Fiber photometry confirmed that VMHdm^{SF1} neurons were persistently activated following rat presentation (ED Fig. 3c–e), with kinetics correlated with thigmotaxis (ED Fig. 3f–i). Accordingly, persistent thigmotaxis could be evoked following optogenetic stimulation of VMHdm^{SF1} neurons (ref⁵ and ED Fig. 2d, e).

We next tested whether VMHdm^{SF1} activity is required for rat-evoked thigmotaxis, using the light-gated chloride channel iC++¹⁵. First, we confirmed that iC++-mediated silencing decreased avoidance of a rat in the home cage (Fig. 1i, j), phenocopying genetic ablation of VMHdm^{SF1} neurons⁵. Next, we silenced these neurons continuously for three minutes during the open field rat exposure test, beginning either five seconds before, or immediately after, rat presentation (Fig. 1l; **“light on,” red vs. green bars**).

Silencing initiated prior to rat exposure prevented the increase in thigmotaxis (Fig. 1l–n; red plots). When silencing was initiated after rat removal, mice exhibited an initial increase in thigmotaxis, but it returned to baseline faster than in controls (Fig. 1l–o, **green plots**; ED Fig. 3a). Thus ongoing VMHdm^{SF1} neuronal activity is essential for maintaining a persistent defensive response to a predator.

To test whether rat-evoked persistent VMHdm^{SF1} activity requires recurrent excitation in these glutamatergic cells, we expressed a Cre-dependent tetanus toxin light chain-GFP fusion (TetTox-GFP) in the neurons to block their neurotransmitter release¹⁶, together with the red calcium indicator jRGECO1a¹⁷ (Fig. 1o). Fiber photometry indicated that TetTox-GFP mice showed significantly faster bulk calcium decay kinetics than control (jRGECO1a/EYFP-injected) mice, following rat exposure (Fig. 1p, r), while the peak response was not affected (Fig. 1q). *Ex vivo* physiology indicated mono- and di-synaptic glutamatergic excitatory connectivity among VMHdm^{SF1} neurons (ED Fig. 4a–d), while electrical stimulation of single VMHdm^{SF1} neurons activated multiple follower cells, as revealed by calcium imaging (ED Fig. 4e–g). These data suggest that local recurrent connectivity, at least in part, underlies VMHdm^{SF1} persistence, but do not exclude a role for feedback from distal targets.

To investigate neural dynamics underlying rat-evoked persistent activity with single-cell resolution, we performed microendoscopic calcium imaging^{18,19} in VMHdm^{SF1} neurons (Fig. 2a–b, ED Fig. 5). Head-fixed mice were imaged on three consecutive days, during ten second presentations with a pseudorandomized set of stimuli (cf. Fig. 1f; n=5 mice, 187.3±8.1 cells imaged per day, 78 cells tracked across days.) Although downsampled VMHdm^{SF1} population responses persisted following rat presentation (Fig. 2c–d), individual neurons showed diverse but reproducible stimulus-evoked dynamics (Fig. 2e–g). While many cells were activated at stimulus onset, others reached their peak only after stimulus removal. Thus, the slow decay of the population response reflects a diverse, time-evolving pattern of activity among individual cells (Fig. 2j–o). These heterogeneous dynamics were confirmed by *in vivo* electrophysiological recordings from VMHdm neurons (ED Fig. 6), excluding an artifact of slow GCaMP6s kinetics. Interestingly, rat and mouse responses were partially overlapping but distinct (Fig. 2h, i). The stimulus selectivity of strongly responsive cells remained stable across days, although some neurons showed progressively decreasing responses suggestive of habituation (ED Fig. 7).

In rodents, non-volatile odor cues can activate neurons of the vomeronasal organ (VNO) for several seconds following inhalation²⁰, raising the possibility that the persistent activity following rat exposure reflected residual kairomones in the nasal mucosa. If so, then we would expect to observe only transient responses to time-resolved non-olfactory stimuli, such as purely visual or auditory cues. VMHdm neurons are not strongly responsive to an overhead visual threat stimulus¹³ (ED Fig. 1). We therefore imaged VMHdm^{SF1} activity in response to an auditory stimulus that evokes defensive behaviours in mice²¹: a series of ultrasonic sweeps (USS) in the ~20 kHz range, typical of rat distress vocalizations (Methods). Prey animals may use predator vocalizations to trigger defensive behavior, a strategy known as “Eavesdropping”²².

The USS strongly and persistently activated VMHdm^{SF1} neurons (Fig. 3a–b). Similar to rat responses, individual VMHdm^{SF1} neurons showed heterogeneous dynamics (Fig. 3c–f). USS-responsive neurons were spatially intermingled with rat-responsive cells, with some responding to both stimuli (Fig. 3g–j). Among neurons responding significantly to at least one stimulus (74.4%), 43.6% responded to only one, and over 70% responded to 2 of the five tested stimuli (Fig. 3k). Most stimulus-responsive VMHdm^{SF1} neurons were excited,

although a few were inhibited (Fig. 3d, l). The first principal component (PC) of population activity reflected stimulus class (rat, mouse, or toy vs. auditory stimuli), while the second PC declined from initial to later trials, perhaps reflecting novelty or salience (Fig. 3n, ED Fig. 7). A 5-way Naïve Bayes decoder was able to predict stimulus identity with above-chance accuracy in held-out trials, across three days of imaging (Fig. 3m). Importantly, stimulus identity also remained decodable for tens of seconds after stimulus onset (ED Fig. 8, 9). Thus, the VMHdm^{SF1} population response can persistently encode the identity of the presented stimulus, even after stimulus removal.

Recurrent network activity, or the release of slow-acting neuromodulators, are often invoked to explain persistent activity^{1,9,10,23–26}. We used computational modeling to investigate whether such mechanisms could account for our observations. We compared four classes of models (Fig. 4a1–4) for their ability to capture two main features of VMHdm^{SF1} activity: its slow dynamics, and its persistent stimulus specificity. The models that best capture these two features combined two elements: inhibition-stabilized recurrent connectivity, and slow excitation (scale of seconds). We call this class of models slow recurrent neural networks (sRNNs) (Fig. 4a3, a4).

To compare model and observed dynamics (Fig. 4b), we computed the autocorrelation matrix of population activity between all pairs of timepoints, t and t' , in a 45 second interval following stimulus presentation (Fig. 4c). We then quantified time-evolving dynamics by taking the mean autocorrelation as a function of the lag between timepoints $|t - t'|$ (Fig. 4d). Several different sRNN models showed autocorrelation dynamics similar to observed dynamics (Fig. 4e). Importantly, models that used slow neuromodulatory transmission alone (Fig. 4a1), or RNNs with NMDA-mediated transmission²⁷ alone (Fig. 4a2), could not match the response dynamics we observed in VMHdm^{SF1} neurons (Fig. 4e1–2); instead both features were required (Fig. 4a3, a4; e3, 5, 6)..

We next investigated which models could also account for the persistent stimulus specificity of VMHdm^{SF1} responses (Fig. 4f). This specificity was quantified as the time-evolving Pearson's correlation between rat- vs. USS-evoked activity (Fig. 4g). Maintaining stimulus specific representations during persistence could be achieved in the sRNN by increasing the gain (strength) of excitatory synapses^{28,29} (Fig. 4a3, h4), but such models failed to match the autocorrelation dynamics of observed activity (Fig. e4). However, both temporal dynamics and stimulus specificity could be matched by one of two models: in the first, the synaptic time constant was increased to 20 seconds (Fig. 4a3, **black, inset**; h5, e5); in the second, connectivity between neuron pairs decreased slightly with distance, and a mild spatial bias was imposed on stimulus-specific inputs (Fig. 4a4, h6, e6; ED Fig. 10). We summarized the performance of our models by creating two “data similarity scores” for each model, quantifying similarity to data in terms of time-evolving dynamics and stimulus specificity; only two models satisfied both conditions (Fig 4i–k, red and black).

Here we provide evidence that slow neural dynamics in the hypothalamus can contribute causally to a persistent defensive emotion state. VMHdm^{SF1} activity, in turn, may activate neuroendocrine processes underlying longer-lasting states⁵. Unlike circulating hormones, however, persistent activity in VMHdm^{SF1} neurons is stimulus-specific, preventing over-

generalization of defensive responses. Such responses may include not only thigmotaxis, but also inhibition of feeding, an anxiety response also controlled by VMHdm^{SF1} neurons³⁰.

The observed slow dynamics can be modeled best by recurrent excitatory networks incorporating fast feedback inhibition and slow neuromodulatory transmission³¹. Feedback inhibition could be provided by threat-activated GABAergic neurons in neighboring DMH³². VMHdm^{SF1} neurons express almost 40 neuropeptides as well as 115 GPCRs³³, properties consistent with optimal model features. However, we cannot exclude alternative cellular mechanisms for slow dynamics, such as K⁺ clearance by astrocytes³⁴. Interestingly, medial amygdala posterioventral (MeApv), an upstream input to VMHdm³⁵, shows non-overlapping responses to different threat stimuli, but these responses are not persistent³⁶; this argues that persistence in VMHdm is not simply inherited from MeApv. However, we cannot exclude a role for meso-scale feedback from VMHdm downstream targets⁴ in maintaining persistence. Nevertheless our data demonstrate, for the first time, that slow neuronal population dynamics in the hypothalamus contributes to the persistence of an emotion state.

METHODS

Anatomical abbreviations.

VNO - vomeronasal organ, AOB - accessory olfactory bulb, MeApv –posteroventral medial amygdala, BNSTif – interfascicular part of bed nucleus of the stria terminalis, VMHdm – doromedial ventromedial hypothalamus, AHN – anterior hypothalamic nucleus, PMd - dorsal preammillary nucleus, PAG - periaqueductal gray, Thal – thalamus, LA – lateral amygdala, BS – brain stem, BLA – basolateral amygdala, CEA – central amygdala.

Animals.

All experimental procedures involving the use of live animals or their tissues were performed in accordance with the NIH guidelines and approved by the Institutional Animal Care and Use Committee (IACUC) and the Institutional Biosafety Committee at the California Institute of Technology (Caltech). SF1-Cre mice were obtained from Dr. Brad Lowell³⁷ and maintained as heterozygotes in the Caltech animal facility as described previously; the SF1-Cre line is also available from the Jackson Laboratory (Stock No: 012462). An account of the specificity of SF1-Cre expression within VMH and characterization of neurons labeled by Cre-expression can be found in⁵.

Heterozygous or wild-type littermate male mice, aged between 8 to 20 weeks, were used in this study. Because hypothalamic nuclei such as VMH show sexually dimorphic gene expression^{38–40}, it is possible that the functional role of VMHdm^{SF1} neurons is sex-specific and that it varies with the estrous cycle. We therefore chose to perform all experiments in male mice, to be consistent with our previous characterization of VMHdm^{SF1} neurons⁵. The study of VMHdm^{SF1} function in females is of obvious interest⁴¹, but requires systematic characterization of the effect of estrous cycle phase on the behavior of interest.

All mice were housed in ventilated micro-isolator cages in a temperature- and humidity-controlled environment under a reversed 12-hour dark-light cycle, and had free access to

food and water. Mouse cages were changed weekly on a fixed day on which experiments were not performed. Long-Evans rats (for use as predators) were obtained from Charles River at 2–3 months of age, and raised to 5–10 months in the Caltech animal facilities.

Virus.

AAV1.Syn.Flex.GCaMP6s.WPRE.SV40 (CS1113) was obtained from the Penn Vector Core. AAV5.EF1a.DIO.iC++.eYFP and AAV2.EF1a.DIO.hChR2.eYFP.WPRE.pA were obtained from the University of North Carolina Vectors Core.

For *ex vivo* electrophysiology and Ca²⁺ imaging studies of VMHdm^{SF1} neurons, *SF1Cre*^{-/-} male mice were injected in VMHdm with 200 nL of of AAV9-Syn-FLEX-jGCaMP7s-WPRE (addgene 104491-AAV9) 5.3×10^{12} genomic copies per mL and AAV5-Syn-FLEX-rc[ChrimsonR-tdTomato] (addgene 62723-AAV5) 1.1×10^{12} genomic copies per mL.

Surgery.

Mice 8–20 weeks old were anesthetized with 5% isoflurane and mounted in a stereotaxic apparatus (Kopf Instruments). 1% - 1.5% isoflurane was used to maintain the anesthesia throughout the surgery procedure. An incision was made to exposure the skull and small craniotomies were made dorsal to each injection site with a stereotaxic mounted drill. Virus suspension (~600 nl) was injected to the VMHdm/c (ML +/- 0.5, AP -4.65, DV -5.6) at a rate of 60 nl/minute using a pulled glass capillary (~40 µm inner diameter at tip) mounted in a nanoliter injector (Nanoliter 2000, World Precision Instruments) controlled by a four channel micro controller (Micro4, World Precision Instruments). Capillaries were kept in place for 10 minutes following injections to allow the adequate diffusion of virus solution and to reduce the virus backflow during capillary withdraw.

For fiber photometry, a custom-made unilateral fiber cannula (400 µm in core diameter, 0.48 NA, Doric Lenses) was implanted after virus injection (ML +/-0.4, AP -4.65, DV -5.4). Metabond (Parkell) and dental cement (Bosworth) were applied to secure the implanted ferrule and cover the exposed skull. For optogenetics, a custom-made bilateral fiber cannula aimed 500 µm above each injection site (200 µm in core diameter, 0.37 NA, Doric Lenses) was implanted and held in place with Metabond and dental cement.

For *in vivo* silicon probe recordings, SF1-Cre mice 8–12 weeks old were anesthetized with 5% isoflurane and mounted in a stereotaxic apparatus. 1%–5% isoflurane was used to maintain the anesthesia throughout the surgery. An incision was made to exposure the skull. A craniotomy window (500 µm x 500 µm, center: ML: +0.3, AP: -4.65) was made on the right hemisphere above the recording site and covered with a thin layer of silicone adhesive compound (WPI) for protection. A custom-made head-bar was leveled and attached to the skull using Metabond. Another small craniotomy was made on the contralateral hemisphere for the insertion of reference wire during recording.

Surgery for microendoscopic imaging was performed as previously described¹⁹. Briefly, we first performed a series of titration experiments of the original viral stock, to determine the virus concentration at which the brightest cytoplasmic but non-nuclear GCaMP6s expression could be observed in slices of fixed brain tissue of the injected mice 4 weeks after injection.

The optimal viral dilution was then used to inject mice for *in vivo* imaging as described above. 2–3 weeks after viral injections, mice were implanted with a graded-index (GRIN) lens (diameter - 0.5 mm, length - 8.4 mm, catalogue #1050–002212, Inscopix) using a supporting device (Proview Implant Kit, cat# 1050–002334, Inscopix). The implantation depth of the lens was determined based on the live visualization of (anesthetized) neural activity as the lens was inserted. Metabond was used to stabilize the lens, and Kwik-Sil sealant (World Precision Instruments) was used to cover the lens surface. After another 2–3 weeks, mice were anesthetized for placement of a microendoscope baseplate (cat# 1050–002192, Inscopix) and a baseplate cover (catalogue #1050–002193, Inscopix) was used to protect the lens when not in use. Five out of twenty implanted animals were selected for *in vivo* imaging studies based on clarity of cytoplasmic GCaMP6s expression.

Stimuli Presentation.

Stimuli were presented either in the mouse's home cage or in a head-fixation set up. In the home cage, a hand-held anesthetized rat weighing 400–600 g was brought in close proximity to the mouse. A stuffed toy rat of approximately the same size as the live rat was used as a control. For the head-fixed preparation, the mouse was placed on a plastic running wheel (15.5 cm diameter) and stabilized by the head-plate (World Precision Instruments, Catalogue #503617) with a custom made tethering system. Animals were habituated to the head-fixation setup for 1 hour each day for 2–3 days before experiments began. Physical stimuli (an awake behaving rat, a conspecific BALB/6 male mouse or a toy rat) were each presented inside a small wire mesh cage, which was held by the experimenter in front of the experimental mouse. Auditory stimuli were presented at 85 dB SPL from above the animal. The ultrasound stimulus (USS) consists of repeated 100 ms frequency sweeps from 17–20 kHz, as described previously²¹. A pure tone of 2 kHz was used as a control. Rat urine was collected in-house and kept at 4°C for up to two weeks. A cotton swab soaked with 100 µl of rat urine or water was presented in front of the experimental mouse. 500 ms looming stimulus was displayed on an overhead screen above the mouse home cage 10 times with 500 ms inter stimulus interval. All stimuli were pseudo-randomized and presented for 10 seconds unless otherwise clarified, with an inter-trial interval of at least five minutes. For microendoscopic imaging, two trials for each stimulus were presented on each of three consecutive days.

Optogenetic manipulation.

Optogenetic experiments were performed as described in⁵. Animals were briefly anaesthetized by isoflurane to connect the fiberoptic patch cord to the bilateral implanted optic cannula (Doric Lenses). Mice were then allowed to recover for at least 15–20 minutes in their home cage before being transferred to the behavioral testing room. Light for both iC ++ and ChR2 activation was delivered via a 473nm laser (Shanghai Laser) controlled by a signal generator (A-M systems, isolated pulse stimulator). The laser intensity for optogenetic stimulation was between 1 and 1.25 mW/mm², and was calibrated at the distance of 0.5 mm below the implanted fiber tip. Three minutes of continuous photostimulation was used for iC ++ activation; 10 seconds (20 Hz, 20 ms pulse width) pulse trains was used for ChR2 activation.

Home cage rat exposure assay.

The mouse home cage was placed into a custom made testing apparatus (35 × 40 × 40 cm), and video of behavior was collected from a side-view camera. After a 6 minute baseline, a predator rat in a cage with a mesh wall (10 × 20 × 35 cm) was placed at one end of the mouse home cage. Ethovision XT software was used to track mouse position and quantify time spent in proximity to the rat.

Open field rat exposure assay.

The mouse was placed in a plastic open top arena (50 × 50 cm, 30 cm walls), with behavior captured using an overhead mounted camera. Following a 10 minute baseline, a rat held in a cage with a mesh wall was held in close proximity to the mouse for 15 seconds, and then removed. Behavior of the mouse was then recorded for an additional 6 minutes. For behavior quantification, Ethovision tracking data was segmented into 30-second chunks, and percent of time spent in the “edge zone” (within 4cm of arena walls) was quantified. For bar graphs in Fig 1n, we define before rat = average over a window from -1 to 0 min relative to rat presentation, after rat = average from 0-1 min after the rat was removed, and after PS off = average from 3-4 min after rat was removed. Anxiety behaviors for Fig 1o were defined as thigmotaxis, immobility, and jumping (escape attempts) and were manually annotated at 30Hz. Pre and post windows correspond to -3 to 0 and 0 to 3 min, respectively, relative to rat presentation.

Tetanus toxin light chain + jRGECO1a imaging.

SF1-Cre mice 8-12 weeks old were anesthetized with 5% isoflurane and mounted in a stereotaxic apparatus. 1%-5% isoflurane was used to maintain the anesthesia throughout the surgery. An incision was made to expose the skull and small craniotomies were made bilaterally with a stereotaxic mounted drill. For the TetTox group, 400 nl viral cocktail (AAV-EF1a-DIO-GFP-TetTox-WPRE, titer: 6×10^{12} genomic copies per mL and AAV-syn-FLEX-NES-jRGECO1a-WPRE, titer: 6×10^{12} genomic copies per mL) was injected bilaterally into VMHdm/c (ML+/- 0.5, AP -4.65, DV -5.5) at a rate of 40 nl/minute. For the control group, 400 nl viral cocktail (AAV-EF1a-DIO-GFP-WPRE, titer: 6×10^{12} genomic copies per mL and AAV-syn-FLEX-NES-jRGECO1a-WPRE, titer: 6×10^{12} genomic copies per mL) was injected bilaterally into VMHdm/c, in the same manner. After injections, a custom-made unilateral fiber cannula (400 um in core diameter, 0.48 NA, Doric lenses) was implanted (ML+/- 0.5, AP -4.65, DV -5.4) on the right injection side and secured with Metabond (Parkell). A head-bar was installed in the same surgery. After four weeks' recovery, fiber photometry was performed in head-fixed mice to examine VMHdm^{SF1} neuron responses to a live rat presented in a cage with mesh wall. Two LEDs modulated at different frequencies (565 nm and 405 nm, Thorlabs) were used to excite RGECO-expressing neurons via the implanted optical fiber. Data processing was the same as for GCaMP6s-based fiber-photometry recordings.

Fiber photometry data acquisition and processing.

Fiber photometry was performed as described in⁴². Briefly, two LEDs modulated at different frequencies (490 nm and 405 nm, Thorlabs) were used to excite GCaMP6s-expressing

neurons via implanted optical fiber. Excitation light at 490 nm activates GCaMP6s in a calcium-dependent manner, while excitation at 405 nm activates GCaMP6s in a calcium-independent manner, thus the 405nm signal can be used to control for bleaching and movement artifacts in the 490nm channel. A photometer (Newport Femtowatt Photoreceiver) received GCaMP6s fluorescent signals, and custom-designed software separated the signals generated by the two LEDs. The output power of both LED was set between 30–50 μ W at the fiber tip to obtain an optimal baseline fluorescence without photobleaching.

To calculate F/F of the 490nm signal, we normalized it to the 405nm baseline as in⁴². The 405nm signal was scaled to match the amplitude of the 490nm signal using linear regression, and F/F computed as (490nm signal – scaled 405nm signal) / (scaled 405 nm signal).

Ex vivo electrophysiology data acquisition and processing.

Acute mouse brain slices were prepared using a vibratome (Leica VT1000S). Slices were cut to 300 μ m thickness and were continuously perfused with oxygenated aCSF containing (in millimolar): NaCl (127), KCl (2.0), NaH_2PO_4 (1.2), NaHCO_3 (26), MgCl_2 (1.3), CaCl_2 (2.4), and D-glucose (10). Whole-cell current- and voltage-clamp recordings were performed with micropipettes filled with intracellular solution containing (in millimolar), K-gluconate (140), KCl (10), HEPES (10), EGTA (10), and Na_2ATP (2), pH 7.3 with KOH. Recordings were performed using a Multiclamp 700B amplifier, a DigiData 1440 digitizer, and pClamp 11 software (Molecular Devices). Slow and fast capacitive components were semi-automatically compensated. Access resistance was monitored throughout the experiments, and neurons in which the series resistance exceeded 15 M Ω or changed $\geq 20\%$ were excluded from the statistics. The liquid junction potential was 10.1 mV and not compensated. Recordings were acquired at 20 kHz. Photostimulation evoked excitatory currents were sampled at the reversal of Cl^- ($V_{\text{HOLD}} = -70$ mV). All recordings were performed at near-physiological temperature ($33 \pm 1^\circ\text{C}$). Reagents used in slice electrophysiology experiments; NeurobiotinTM tracer (Vector laboratories) was used in combination with Streptavidin conjugated to Alexa Fluor 647. MATLAB and OriginPro9 were used for electrophysiological data analysis.

Cell filling and reconstruction.

Mouse VMHdm^{SF1} neurons were recorded in whole-cell mode with intracellular pipette solution as above, with the addition of 0.2% neurobiotin. After recording, slices were placed in fixative (4% paraformaldehyde/0.16% picric acid), washed in PBS and incubated at 4°C for 72h in a solution containing streptavidin conjugated to Alexa Fluor 647. After extensive washing, slices were mounted with 2.5% DABCO in glycerol. VMHvl^{SF1} neuron identity of all filled cells was confirmed with colocalization studies between Neurobiotin and virally-induced jGCaMP7s expression.

Ex vivo Ca^{2+} imaging.

The activity of mouse VMHdm^{SF1} neurons was monitored by imaging fluorescence changes of the jGCaMP7s biosensor, using a CCD camera (Evolve® 512, Photometrics), mounted on an Olympus BX51WI microscope. A 60x water-dipping objective was used to focus on

VMHdm. Ca^{2+} imaging analysis was performed using the MIN1PIPE one-photon based calcium imaging signal extraction pipeline⁴³, in combination with custom-written MATLAB routines. Synchronized acquisition of electrophysiology and imaging data sets was achieved using the “frames out” digital output of the Evolve 512 camera and the START digital input in the DigiData 1440A.

Ex vivo optogenetics.

Photostimulation during *ex vivo* whole-cell recordings was performed via a 4.1 watt 621 nm LED mounted on the microscope fluorescence light source and delivered through the 60X objective's lens. Photostimulation was controlled via the analog outputs of a DigiData 1440A, enabling control over the duration and intensity. The photostimulation diameter through the objective lens was $\sim 310 \mu\text{m}$ with illumination intensity typically scaled to $0.30 \text{ mW}/\text{mm}^2$.

Confocal microscopy.

Brain slices were imaged by confocal microscopy (Zeiss, LSM 800). Brain areas were determined according to their anatomy using Paxinos and Franklin Brain Atlas⁴⁴.

Silicon probe *in vivo* electrophysiology data acquisition and processing.

After one to two days' recovery from surgery, extracellular recordings were made in VMHdm in five awake head fixed mice using 64-channel silicon probes⁴⁵ (UCLA, Masmanidis lab, model 64G). The probe shanks were coated with fluorescent dye for later visualization of the recording site. Two recording sessions were performed on each mouse on two consecutive days. During each recording session, a live rat held in a cage with mesh wall was presented to the head-fixed mouse for ten seconds/trial for five trials. Signal was sampled at 30 kHz and acquired using Open Ephys platform. Single units were isolated using Kilosort offline.

To identify rat-responsive units, we defined a pre-stimulus baseline in a 10 second window prior to the stimulus presentation, and defined responsive units as those units for which the average firing rate for any one-second window in the first 30 seconds after stimulus presentation was more than three standard deviations above the mean of the baseline firing rate. Spontaneous firing rate of each unit is defined as the mean firing rate during the 10 second baseline.

Microendoscopic imaging data acquisition and processing.

We used a head-mounted miniaturized microscope (nVista, Inscopix) for calcium imaging. Pilot experiments were done to identify imaging parameters that produced the clearest signal to noise ratio while limiting photobleaching. All mice except one were recorded at 11 Hz with 90.0ms exposure time, 10–20% LED illumination and 1.5 – 2.5x gain; the remaining mouse was imaged at 20Hz with 50ms exposure time. A custom-built system was used to synchronize the cameras for behavioral recordings and devices for neural recordings and stimuli delivery.

Imaging frames were spatially downsampled by a factor of two in the X and Y dimensions, and spatially high-pass filtered with a cutoff spatial frequency of 40 μm . All frames collected over the course of a single day were then concatenated into a single stack and registered to each other to correct for motion artifacts using a rigid-body transformation (TurboReg plugin for ImageJ). Single cell Ca^{2+} activity traces and spatial filters were extracted from the registered movie using CNMF-E⁴⁶. Because CNMF-E can identify sources of variance other than neurons (particularly signals like motion artifacts or neuropil fluorescence⁴⁷), extracted traces and ROIs were manually screened to remove neuropil or other non-neuronal signals. Non-neuronal signals can be visually identified by a lack of a round, soma-like shape in their ROIs: most of these were large and diffuse ROIs or had evidence of motion artifacts in their corresponding traces. The cleaned set of cells were then registered across three consecutive days of imaging as described in¹⁹. Briefly, all extracted spatial filters from a given day of imaging were added to create a cell map, and intensity-based image registration was used to identify a pair of rigid-body transformations to align the day 1 and 3 maps to the day 2 maps. Overlapping triplets of spatial filters for the three days were identified by finding cells on day 1 and 3 with the smallest Euclidean distance to each day 2 cell. All identified triplets were then manually screened for accuracy. Roughly half of all cells could be registered across all three days of imaging.

Statistics.

Data met the assumptions of the statistical tests used and were tested for normality and variance. Normality was determined by D'Agostino–Pearson normality test. *t*-test was performed using either GraphPad Prism software (GraphPad Software Inc.) or MATLAB (Mathworks Inc). Statistical significance was set at * = $P < 0.05$, ** = $P < 0.01$, *** = $P < 0.001$, **** = $P < 0.0001$. Sample sizes were not pre-selected for statistical power. Experimenters were not blinded to animal condition.

Units of neuronal activation.

Stimulus-evoked responses of VMHdm^{SF1} neurons are reported in units of baseline standard deviation, σ , defined as the standard deviation of observed fluorescence in a 30-second pre-stimulus baseline.

Fitting decay constants in fiber photometry and population average microendoscope data.

The stimulus-evoked response of the SF1⁺ population could be well fit by a difference of exponentials of the form $K(t) = A(\tau_{decay} - \tau_{rise})^{-1} (e^{-t/\tau_{rise}} - e^{-t/\tau_{decay}})$ where t is time in seconds, and A , τ_{decay} , and τ_{rise} are fit parameters characterizing the amplitude and kinetics of the response. Values of τ_{decay} , and τ_{rise} were fit for each trial to minimize the mean squared error between $K(t)$ and the SF1⁺ population response over a 30 second window following the start of stimulus presentation, using the *fminunc* function in Matlab.

Identifying stimulus-responsive cells.

Some analyses, such as calculation of time to peak or half-peak strength of stimulus preference, were performed only on cells that showed a significant response to the stimulus or stimuli in question. For these analyses, we defined a pre-stimulus baseline as the F/F in

a ten-second window prior to stimulus presentation, and defined responsive cells as those neurons for which the average $\Delta F/F$ value for any one-second window in the first 30 seconds after stimulus presentation was more than four standard deviations above the mean of baseline activity on that trial. Only cells that passed this criterion on both trials within a day were included for analysis.

Finding peak and decay to half-peak times.

The time of the peak population response was defined as the first time (relative to start of stimulus presentation) the population $\Delta F/F$ passed 95% of its maximum observed value on a given trial. The time to decay to half-peak was defined as the last time the population $\Delta F/F$ was above 50% of its maximum value relative to pre-stimulus baseline. This analysis was performed separately for each cell on each day of imaging, using only stimulus-responsive cells (see above); values were averaged across two repeated stimulus presentations.

Strength of cell preference.

The strength of cell preference for either of a pair of stimuli (Fig 2g and Fig 3i,k) was defined as $(s_a - s_b) / (|s_a| + |s_b|)$, where s_a and s_b are the average $\Delta F/F$ of that cell in a 45-second window following stimulus onset, for stimulus pair a vs b (eg rat vs USS). This analysis was performed separately for each cell on each day of imaging, using only cells that responded to either one (or both) of the two stimuli, as defined above; values of s_a and s_b were averaged across two repeated stimulus presentations.

Decoder analysis.

Stimulus identity was decoded from the activity of all SF1⁺ neurons that could be reliably tracked across three days of imaging, using a two-class or five-class cross-validated Naïve Bayes decoder (*fitcnb* in Matlab). Bar plots of decoder accuracy (Fig 3n) and confusion matrix (ED 7a) were generated using held-out test data for a five-class Naïve Bayes decoder trained on the time-averaged responses of imaged neurons in a window from 30 seconds before to approximately 60 seconds after stimulus presentation. Time-evolving plots of decoder accuracy (Fig 3o, ED 8b–c) were constructed by training a separate cross-validated decoder on the time-averaged activity of imaged neurons in a one-second window, for each one-second window from 10 seconds before to 30 seconds after stimulus presentation. Decoder performance is reported as the average prediction accuracy on held-out test data; chance accuracy is 1/2 for the two-class decoder and 1/5 for the five-class decoder.

Stimulus-evoked autocorrelation.

We constructed the standard correlation matrix C of VMHdm^{SF1} cell activity, defined as the pairwise correlation coefficient between all columns of a neurons \times time matrix of imaged activity. Values in C were averaged across each trial for a given stimulus over three days of imaging, and then averaged across $n=5$ imaged mice, for all imaging frames from zero to 45 seconds relative to the onset of stimulus presentation (imaging framerate was 11 Hz). The mean correlation for lag t was computed by averaging $C(x, x+t)$ for all x between 0 and $45-t$ seconds.

The same calculation was used for simulated data, with correlations computed every 10 simulation time steps (10ms). To make values comparable to the experimental data, model cell spikes were convolved with a pair of exponential filters with time constants of 0.5 seconds and 1.5 seconds, simulating the kinetics of the GCaMP6s response.

Rat/USS Pearson's correlation.

The Pearson's correlation between rat and USS responses was computed for each mouse using the trial-averaged response of all neurons on the first day of imaging. Pearson's correlation was computed between the vectors of population activity from 10 seconds before to 30 seconds after stimulus onset, sampled at 11Hz (acquisition frequency).

For simulated data, the "rat" and "USS" inputs were assumed to be excitatory inputs to a randomly selected fraction of neurons in the model (temporal structure of stimulus and percent of neurons receiving input specified below for each model). Pearson's correlation between these two stimuli was computed across all model cells that fired 10 or more spikes across the two stimuli. GCaMP6s kinetics were simulated as for the stimulus-evoked autocorrelation analysis.

Slow neuromodulation model.

For this model we assumed that VMHdm^{SF1} neuron dynamics were determined entirely by long-lasting peptidergic input, and that there were no recurrent connections between neurons within VMHdm. Given a model population of $N = 1000$ neurons, we assumed that a random 10% of neurons received peptidergic input for any given stimulus. For cells receiving stimulus-evoked input, we modeled the firing rate $r_i(t)$ of neuron i as $r_i(t) = g * p_i(t)$, where $g \sim U(0,60)$ sets the strength of excitatory peptidergic input onto neuron i and $p_i(t)$ is a stimulus-evoked peptide-mediated excitatory current. Dynamics of $p_i(t)$ evolve as $\tau_p dp_i/dt = -p_i(t) + \delta(t)$, where $\delta(t)$ is the delta function and $\tau_p = 25$ sec, the decay time constant that sets the duration of peptidergic excitation, was set to match the observed decay time constant of the population average VMHdm^{SF1} response. To simulate spiking, the firing rate $r_i(t)$ was used to set the instantaneous rate constant of a non-homogeneous Poisson process with a simulation time step of $dt = 1$ ms.

Spiking recurrent neural network model + NMDA.

We constructed a model population of $N = 1000$ standard current-based leaky integrate-and-fire neurons, in which each neuron has membrane potential x_i characterized by dynamics $\tau_m dx_i/dt = -x_i(t) + I(t)$, where $\tau_m = 20$ ms is a membrane time constant and I (specified below) is a combination of external and recurrent inputs. To model spiking, we set a threshold θ (typically $\theta = 0.1$) such that when the membrane potential $x_i(t) > \theta$, $x_i(t)$ is reset to 0 and instantaneous spiking rate $r_i(t)$ is set to 1. Spiking-evoked input to postsynaptic neurons was modeled as a synaptic current with dynamics $\tau_E dp_i/dt = -p_i(t) + r_i(t)$, where τ_E is the decay time constant of excitatory currents. To simulate the slow excitatory currents produced by NMDA receptors, we set $\tau_E = 200$ ms.

We next added recurrent connectivity between model units. Connectivity between model units is random and sparse, with $p = 10\%$ probability of a synapse forming between any two

neurons, and weights of existing synapses sampled from a uniform distribution: $W_{ij} \sim U(0, 1/(Np)^{1/2})$. We also defined a gain parameter g that scales the strength of all synapses in the network.

To reduce finite-size effects in this model, we modeled recurrent inhibition by a single graded input I_{inh} representing an inhibitory population that receives equal input from, and provides equal input to, all excitatory units; dynamics of I_{inh} thus evolve as

$$\tau_I \frac{dI_{inh}}{dt} = -I_{inh}(t) + \frac{1}{N} \sum_{n=1}^N r_N(t), \text{ where } \tau_I = 50 \text{ ms is the decay time constant of inhibitory currents.}$$

Each modeled ‘‘stimulus’’ input to the network was modeled with the same dynamics, with a high initial firing rate that decayed to a much lower sustained firing rate, and dropped to zero ten seconds after stimulus onset: specifically, in our model this input took the form

$$s(t) = \mathbb{1}(t < 10) \int_{-\infty}^t \mathbb{1}(0 < t' < 2) e^{-\frac{t-t'}{2}} dt' \text{ where } \mathbb{1} \text{ is the indicator function. Each stimulus drove a random 50\% of excitatory units in the network with input strength } w_i \sim g * U(0, 1).$$

Thus, outside of spiking events, the membrane potential of neuron i evolves as

$$\tau_m \frac{dx_i}{dt} = -x_i(t) + g \left(\sum_{j=1}^N J_{ij} p_j(t) - g_{inh} I_{inh}(t) \right) + w_i s(t). \text{ Model dynamics were simulated in discrete time using first-order Euler's method with a timestep of } dt = 1 \text{ ms; a small Gaussian noise term } \eta_i \sim N(0, 1)/5 \text{ was added at each timestep. We explored model dynamics over a range of values of } g \text{ and } g_{inh} \text{ by selecting a value of } g \text{ and performing a grid search over } g_{inh} \text{ until the desired degree of persistence was achieved. Figures in the paper correspond to } g = 1, g_{inh} = 3.8.$$

Spiking recurrent neural network model + slow excitation (sRNN).

In experimenting with the RNN+NMDA model described above, we found that we could achieve diverse temporal dynamics of spiking neurons if the time constant of excitation (τ_E) was further increased, causing excitation to be much slower than inhibition. This allows model neurons to act as leaky integrators of their excitatory inputs, and start spiking when the population average activity (reflected by inhibitory input) drops below the integrated excitation. We further modified the model by replacing the excitatory current with a mix of fast and slow excitatory neurotransmission; similar results are obtained in a model with just the slow component of excitatory neurotransmission.

The slow excitatory component of our model is open to biological interpretation. One appealing source of slow excitation is peptidergic signaling: our recently published single-cell RNAseq data indicate that VMHdm^{SF1+} neurons collectively express 115 G protein-coupled receptors, including 53 neuropeptide or neurohormone receptors, and 36 neuropeptides³³. However, we also do not rule out alternative potential mechanisms for slow excitation, such as non-peptide neuromodulators or slow potassium clearance from the synapse by astrocytes⁴⁸.

We modeled fast excitatory currents as in the prior model, with dynamics $\tau_{Efast} \frac{dp_{fast,i}}{dt} = -p_{fast,i}(t) + r_i(t)$, however we set $\tau_{Efast} = 50 \text{ms}$ to better match the decay time constant of

glutamatergic excitation. To model slow excitation, we assumed that when a neuron spiked, postsynaptic excitation was contingent on the recent firing rate history of that neuron, with excitation only occurring if the average number of spikes in the last second exceeded a threshold T (typically $T = 20$, although performance was not strongly dependent on this parameter.) That is, the spiking of neuron i evoked excitation if $\int_{t-1}^t r_i(\tau) d\tau > T$. Dynamics of slow excitation were otherwise modeled as before, thus giving

$$\tau_{E_{slow}} \frac{dp_{slow_i}}{dt} = -p_{slow_i}(t) + r_i(t) \cdot \mathbb{1}\left(\int_{t-1}^t r_i(\tau) d\tau > T\right)$$
, where $\mathbb{1}$ is the indicator function. We used $\tau_{E_{slow}} = 6$ sec for all versions of the sRNN except for the third (black traces in Fig 4), for which $\tau_{E_{slow}} = 20$ sec ($\tau_{E_{slow}}$ is abbreviated as τ_S in Fig 4).

For simplicity we assumed the synaptic weight matrix J was the same for both fast and slow components of excitation. Membrane potential dynamics in this model are therefore given by $\tau_m \frac{dx_i}{dt} = -x_i + g \sum_{j=1}^N J_{ij} p_{fast_j}(t) + g \sum_{j=1}^N J_{ij} p_{slow_j}(t) - g_{inh} I_{inh}(t) + w_i s(t)$. We present three versions of this model in Fig 4: in the “low gain” model, $g = 1$, $g_{inh} = 8.8$, $\tau_{E_{slow}} = 6$ sec; in the “high gain” model, $g = 6$, $g_{inh} = 7.8$, $\tau_{E_{slow}} = 6$ sec; in the “high τ_S ” model, $g = 2.5$, $g_{inh} = 4.25$, $\tau_{E_{slow}} = 20$ sec. Simulation was performed as for the NMDA-RNN model, and as above parameters were fit by fixing the value of g (and $\tau_{E_{slow}}$) and performing a grid search over values of g_{inh} to achieve the desired degree of persistence.

sRNN + local connectivity.

The locally connected version of the sRNN model was created by adding a “distance dependence” on the probability of a pair of neurons forming a synaptic connection. Model neurons were numbered between 1 and N , and for neurons i and j the probability of forming a synapse was defined as $p_{ij} = p_0 e^{-(i-j)^2/\sigma}$, where $p_0 = 0.1$ is the baseline degree of connectivity in the network, and σ sets the rate at which connectivity falls off with distance (here distance is defined as $|i-j|$). We found that broad connectivity was necessary to match the stimulus representation overlap seen in the data; plots in Fig 4 and the illustration of distance-dependent connectivity in ED Fig 9a–b were constructed using $\sigma = 0.7N$.

As in the sRNN, each stimulus in the local connectivity model provided input to 50% of model neurons. To match the observed Pearson’s correlation of the data, we found that it was necessary for stimulus inputs to reflect the structure of the model network, by targeting separate but still overlapping portions of the band of model neurons. Specifically, we found that the data was well fit when the middle 50% of model neurons in the band could receive input from both rat and USS stimuli, while the outermost 25% could only receive rat or USS input (see ED Fig 9a).

Data similarity score, time-evolving dynamics.

We constructed a data similarity score to quantify the degree of similarity between the plotted curves in Fig 4e, thus capturing how much the time-evolving dynamics of model neurons looked like that of the data. For each model and each mouse, we computed the Mean Correlation as defined above, which we will call $MC_{model}(t)$ for a given model and $MC_{mouse\ i}(t)$ for a given mouse. MC is a function of time-- thus to quantify the mean

similarity between the data and a given model over time, we considered the value of $MC_{model}(t)$ and $MC_{mouse\ i}(t)$ for all imaging frames (acquired at 11Hz) from 0 to 45 seconds relative to stimulus onset, which we reference using a frame index $t = 1 \dots T$ (so $t = 1$ corresponds to a time of 0 sec and $t = T$ corresponds to a time of 45 sec). Given these definitions, we define the data similarity score of the model dynamics as:

$$\text{Similarity Score}_{\text{dynamics}} = \frac{1}{N} \sum_{i=1}^N 1 - \left(\sum_{t=1}^T |MC_{\text{mouse } i}(t) - MC_{\text{model}}(t)| \right) / \left(\sum_{t=1}^T |MC_{\text{mouse } i}(t)| \right)$$

This can be simply interpreted as akin to the area between the data/model curves for each plot in Fig 4e. Note that the MC for the data here was computed from the USS-evoked neural activity, however MC for other stimuli gave similar results, as we found little difference between the MC for different stimuli.

Data similarity score, stimulus specificity.

This data similarity score quantifies the degree of similarity between the plotted curves in Fig 4h, ie how much the Pearson's correlation between rat- and USS-evoked activity in each model looked like that observed in the data. We computed the Pearson's correlation (as defined above) for each model and each mouse, which we call $PC_{model}(t)$ for a given model and $PC_{mouse\ i}(t)$ for a given mouse. We define frames $t = 1 \dots T$ as all imaging frames from times 0 to 45 seconds relative to stimulus onset (same as for the similarity score of dynamics). We then define the data similarity score of model stimulus-specific activity as:

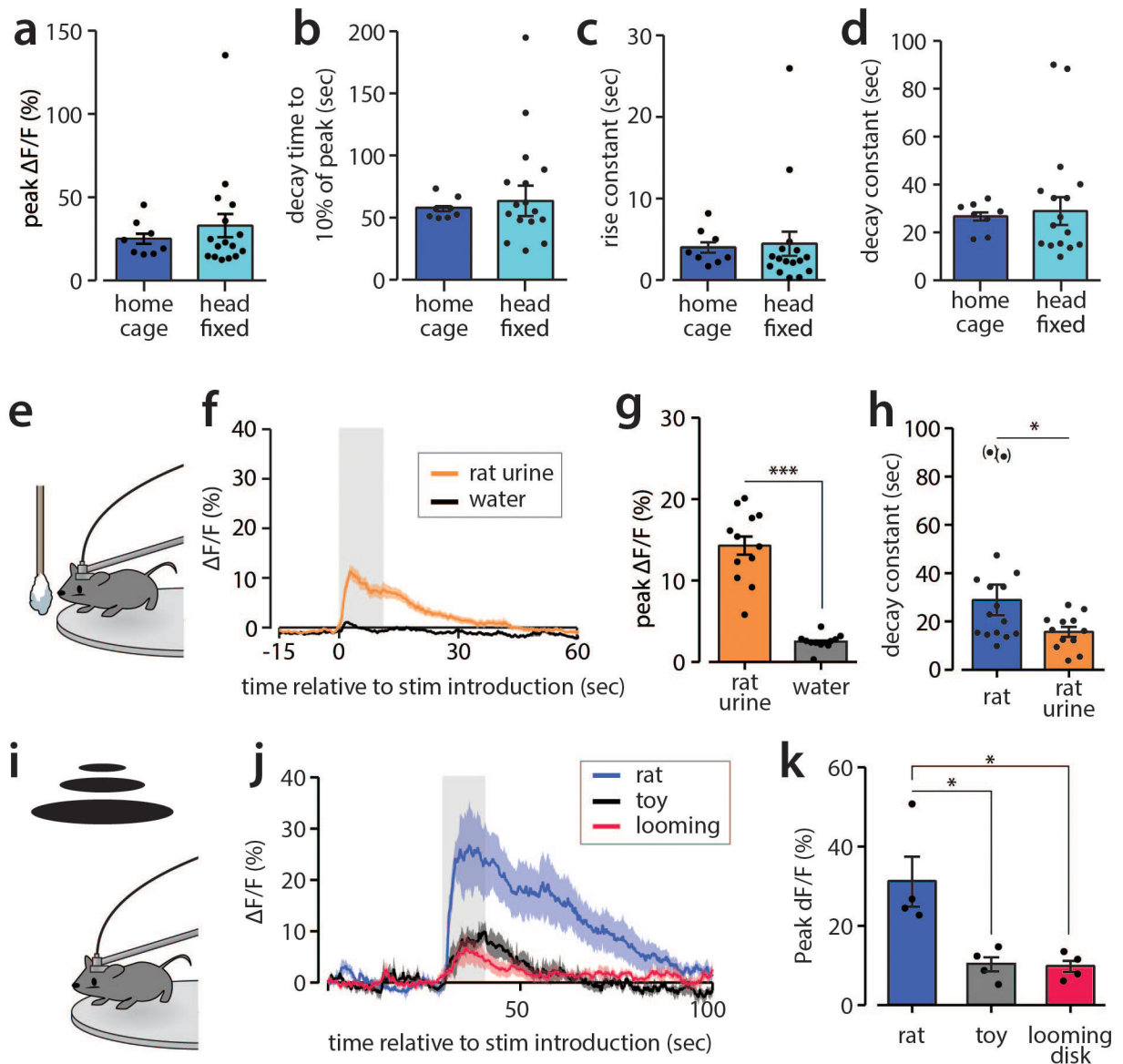
$$\text{Similarity Score}_{\text{specificity}} = \frac{1}{N} \sum_{i=1}^N 1 - \frac{1}{T} \left(\sum_{t=1}^T |PC_{\text{mouse } i}(t) - PC_{\text{model}}(t)| \right)$$

Like the similarity score of the dynamics, this can be interpreted as the area between the data/model curves for each plot in Fig 4h.

Data and code availability.

Code for data analysis and modeling portions of this paper has been made publicly available at https://github.com/DJALab/VMHdm_persistence. The data that support the findings of this study are available from the corresponding author upon reasonable request.

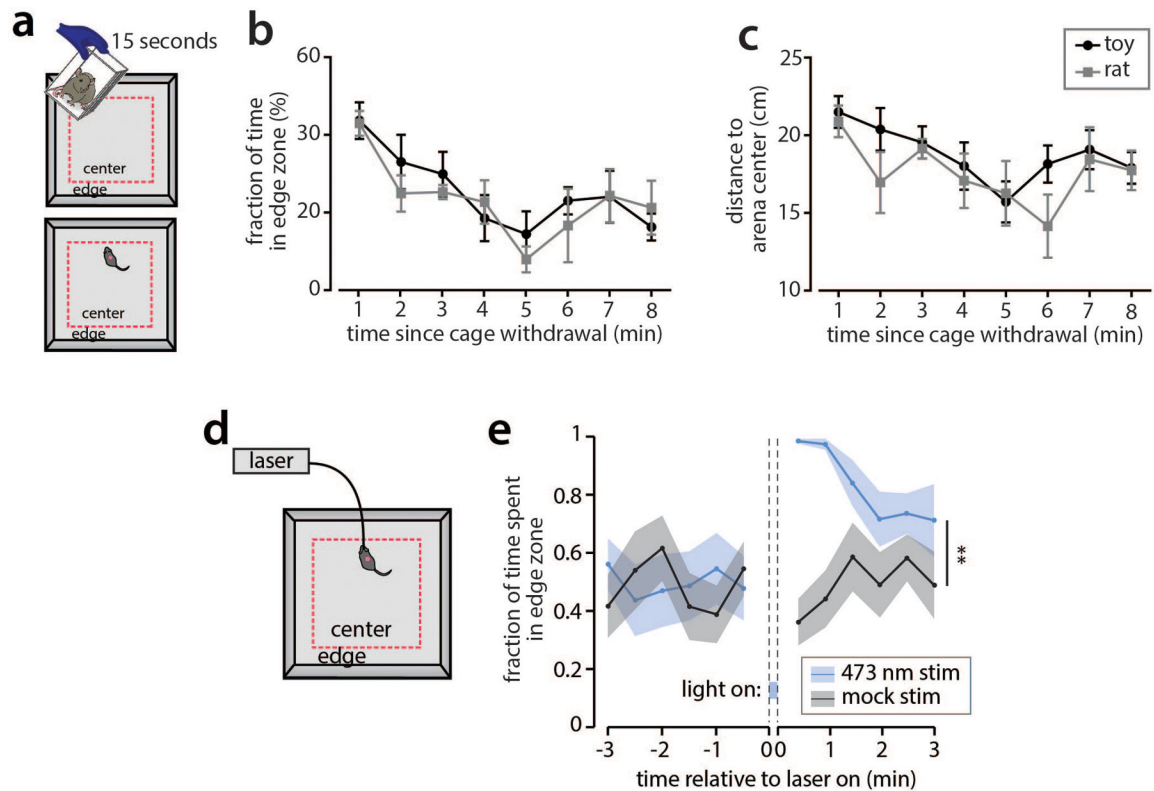
Extended Data



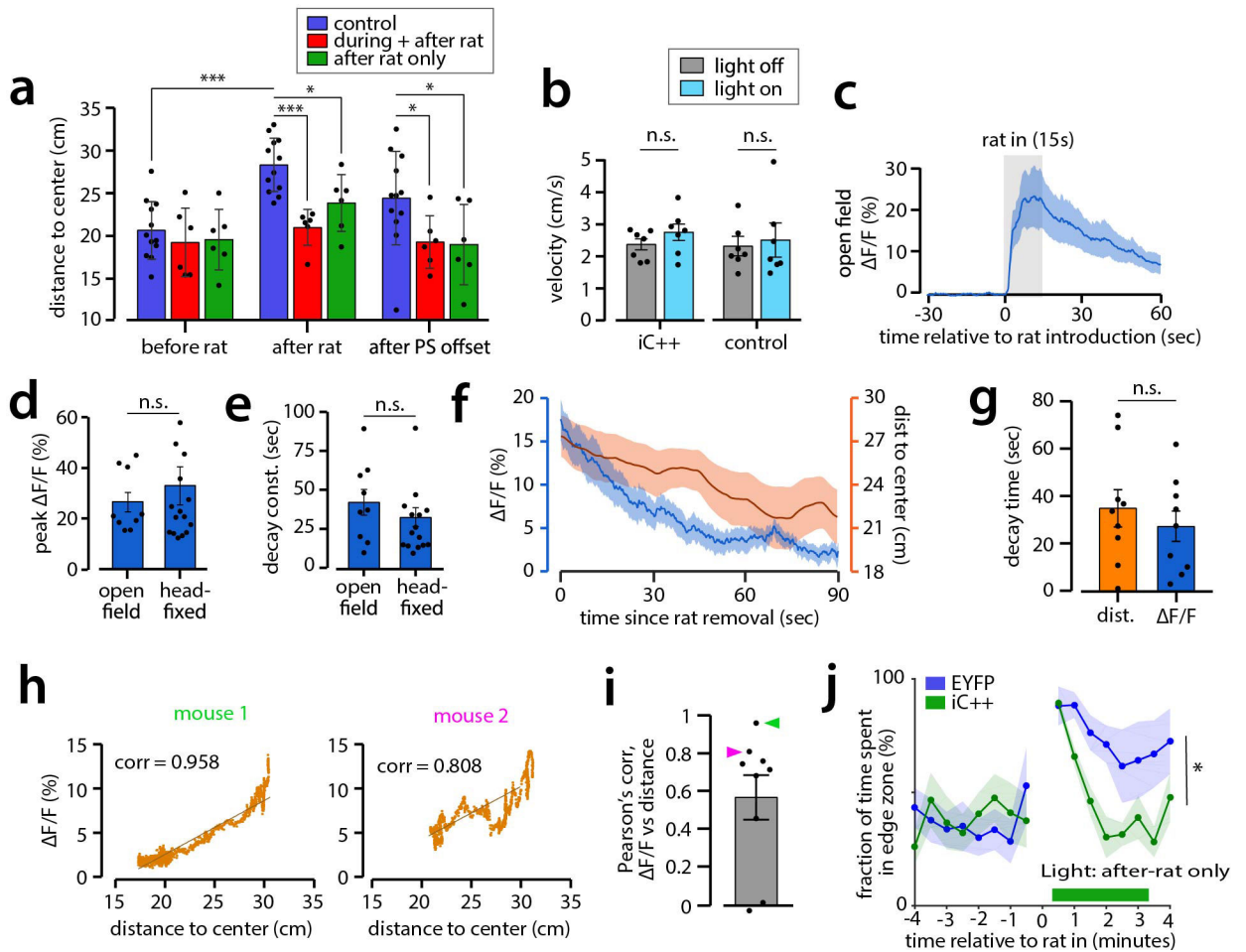
Extended Data 1. Additional properties of SF1⁺ neurons' responses to rat, rat urine, and looming disk stimuli.

a, Peak $\Delta F/F$ activity in response to rat in home cage (anaesthetized, uncaged stimulus) and a head-fixed set-up (awake, caged stimulus). (home cage group n = 4 mice; head-fixed group n = 6 mice; mean \pm SEM). **b**, Decay time to 10% of peak (same mice as **a**; mean \pm SEM). **c**, Rise time constant of rat-evoked activity. (same mice as **a**; mean \pm SEM). **d**, Decay time constant of rat-evoked activity. (same mice as **a**; mean \pm SEM). **e**, Schematic illustrating urine presentation to head-fixed mouse for fiber photometry. **f**, Averaged $\Delta F/F$ activity traces of SF1⁺ neurons in response to rat urine or water (n = 6 mice, 2 trials per mouse; mean \pm SEM). **g**, Peak $\Delta F/F$ activity triggered by rat urine or water. (same mice as **f**; mean \pm SEM). **h**, Decay time constant for rat or rat urine response (n = 8 mice (rat), n = 6 mice (urine), 2 trials per mouse; mean \pm SEM). **i**, Looming disk presentation to head-fixed mouse for fiber

photometry. **j**, F/F response to rat, toy rat, or looming disk stimuli presented for 10 seconds in the animal's home cage ($n = 4$ mice, 1 trial per mouse; mean \pm SEM). **k**, Peak of F/F response to rat, toy rat, and looming disk stimuli. (n same as in **j**; mean \pm SEM).



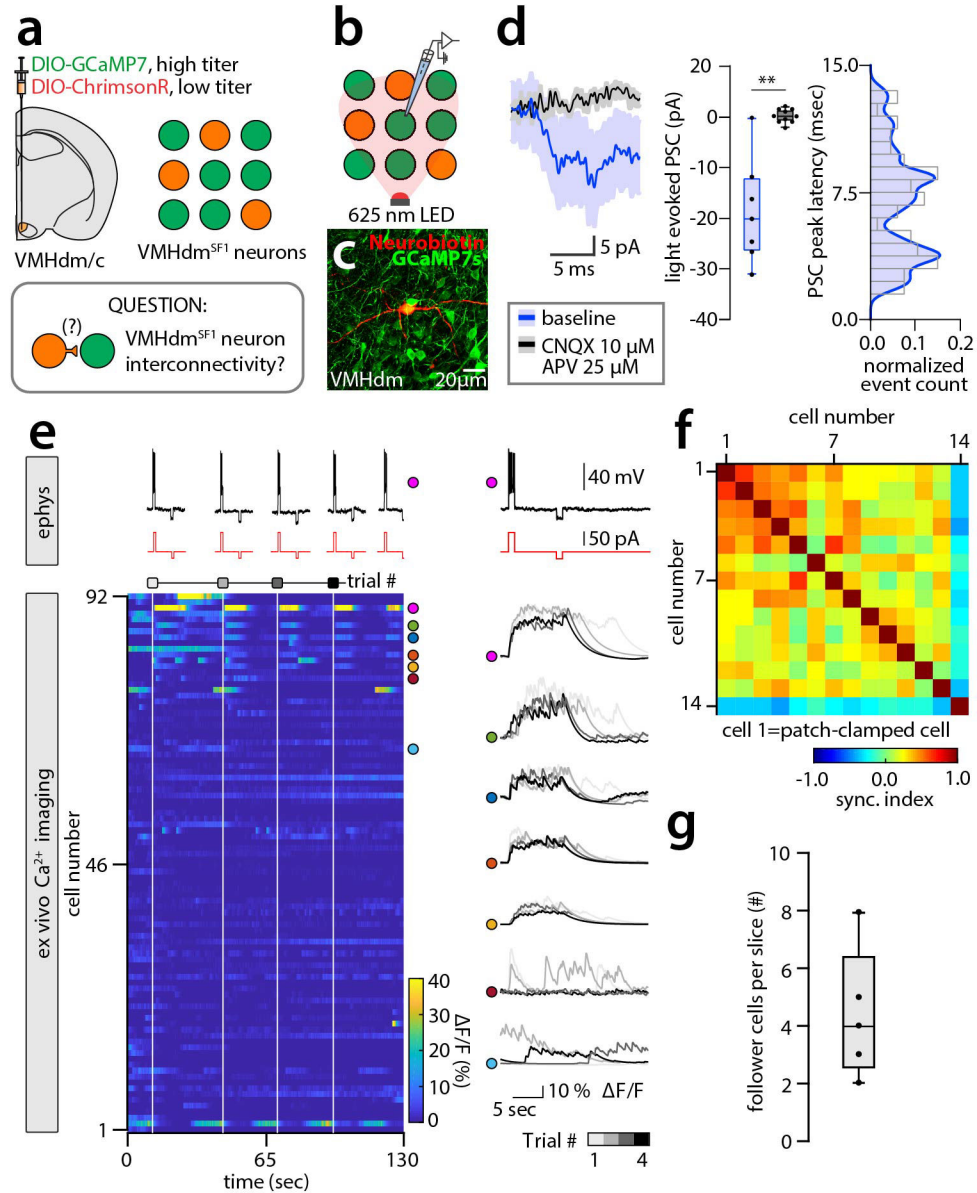
Extended Data 2. No change in mouse behavior due to potential lingering odor from rat.
a, Schematic plot showing experiment protocol: top, a live rat or toy rat (control) was brought to the open field arena in a wire mesh cage for 15 seconds; bottom, mouse was introduced to arena afterwards immediately. **b**, Fraction of time spent in center zone (defined by red dashed line in **a**) for rat group and control group ($n = 6$ for each group; mean \pm SEM). **c**, Distance from mouse body center to arena center. (same mice as **b**; mean \pm SEM). **d**, Schematic plot showing optogenetic activation protocol. Mice expressing ChR2 in VMHdm^{SF1} neurons were introduced to the open field arena. After a five-minute habituation period, a ten-second light or mock stimulation was delivered to the mice. **e**, Fraction of time spent in the edge zone. Dashed lines mark time of rat presentation. ($n = 4$ mice for each group; mean \pm SEM).



Extended Data 3. Fiber photometry and VMHdm^{SF1} neuron silencing in open field rat exposure assay.

a, Distance from mouse body center to arena center during three different time periods: before rat, after rat and after photostimulation offset, corresponding to $-1 - 0$, $0 - 1$ and $3 - 4$ minute intervals in Fig. 1m. (same mice as Fig 1m; mean \pm SEM). **b**, Mean velocity was not altered by photostimulation of iC++ and control (Cre-dependent iC++ virus injected into wild type littermate) mice. Velocity was measured in mouse home cage and averaged during a three-minute period for light off and light on sessions. ($n = 7$ mice). **c**, F/F activity traces (mean \pm SEM) of VMHdm^{SF1} neurons in response to rat presentation in open field arena. Shaded grey bar denotes the 15s presentation of rat ($n = 9$ mice). **d**, Peak F/F activity triggered by awake, caged rat in open field arena ($n = 9$) and head-fixed set up ($n = 8$) (mean \pm SEM). **e**, Decay constants of F/F activity in open field arena compared to head-fixed set up (same mice as **d**; mean \pm SEM). **f**, Comparison of traces (mean \pm SEM) for F/F activity (blue) and the distance from mouse body center to arena center (orange), aligned to time of rat removal. ($n = 9$ mice; distance to center is plotted as a 30-second moving average.) **g**, Decay time measured as the time elapsed to reach 50% of the peak for linearly fitted data. ($n = 9$; mean \pm SEM). **h**, Scatter plot of F/F activity vs. distance from mouse to arena center, fit by linear regression, for two example mice. Mouse 1, $r = 0.958$, $p < 0.0001$; mouse 2, $r = 0.808$, $p < 0.0001$. **i**, Pearson's correlation coefficient between F/F activity and the distance

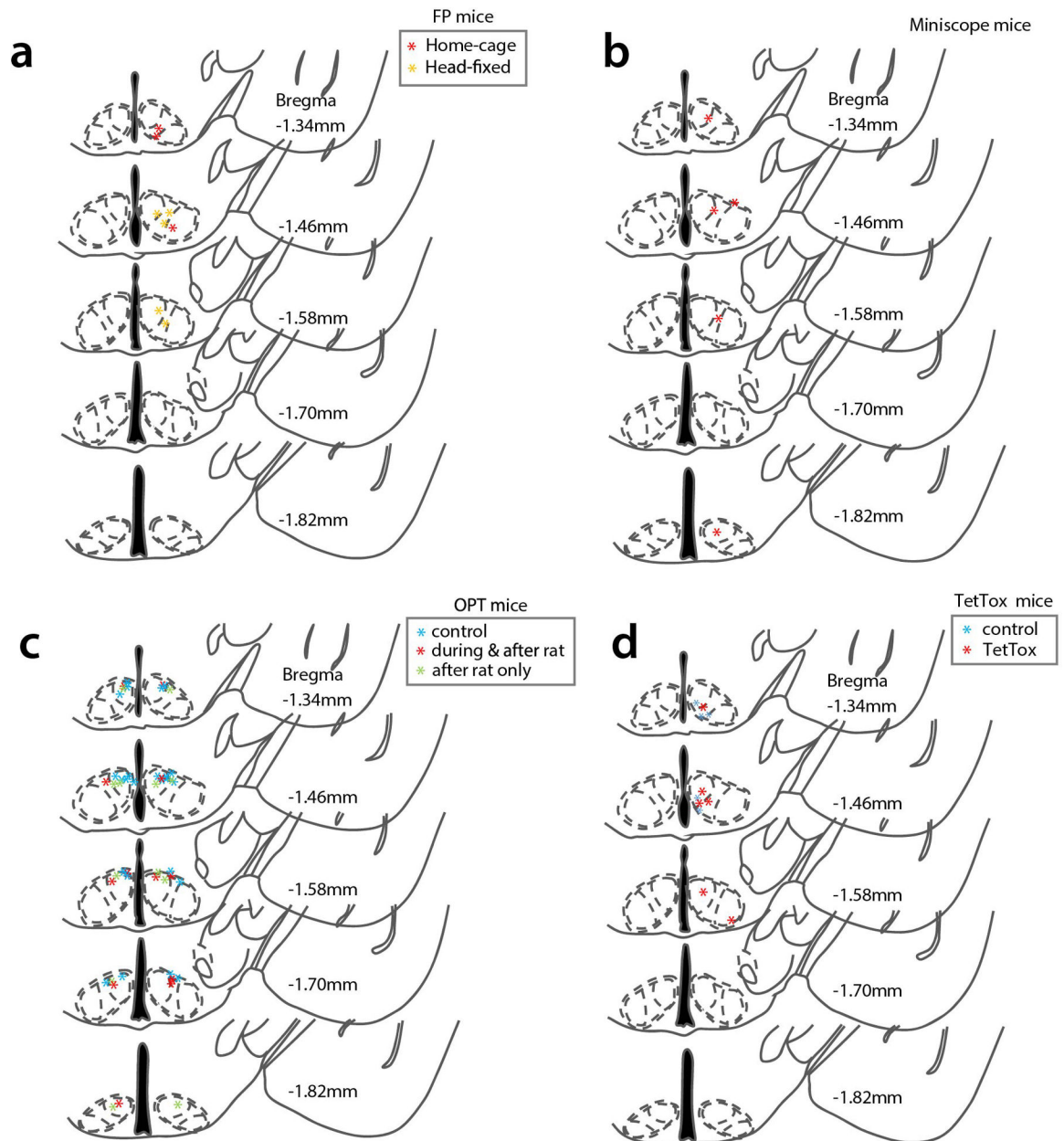
to center, with the two mice plotted in **(h)** indicated by colored arrowheads ($n = 9$ mice; mean \pm SEM). **j**, Additional control for optogenetic loss-of-function experiment (see Figure 1l), using Cre-dependent AAV-DIO-EYFP virus injected into SF1-Cre mice. Green horizontal bar denotes photostimulation period ($n=5$, EYFP group; $n = 6$, iC⁺⁺ group (SF1-Cre mice injected with AAV-DIO-iC⁺⁺). Repeated measures ANOVA test, mean \pm SEM.)



Extended Data 4. Excitatory monosynaptic interconnectivity in VMHdm^{SF1} neurons, sensitive to glutamate receptor blockade.

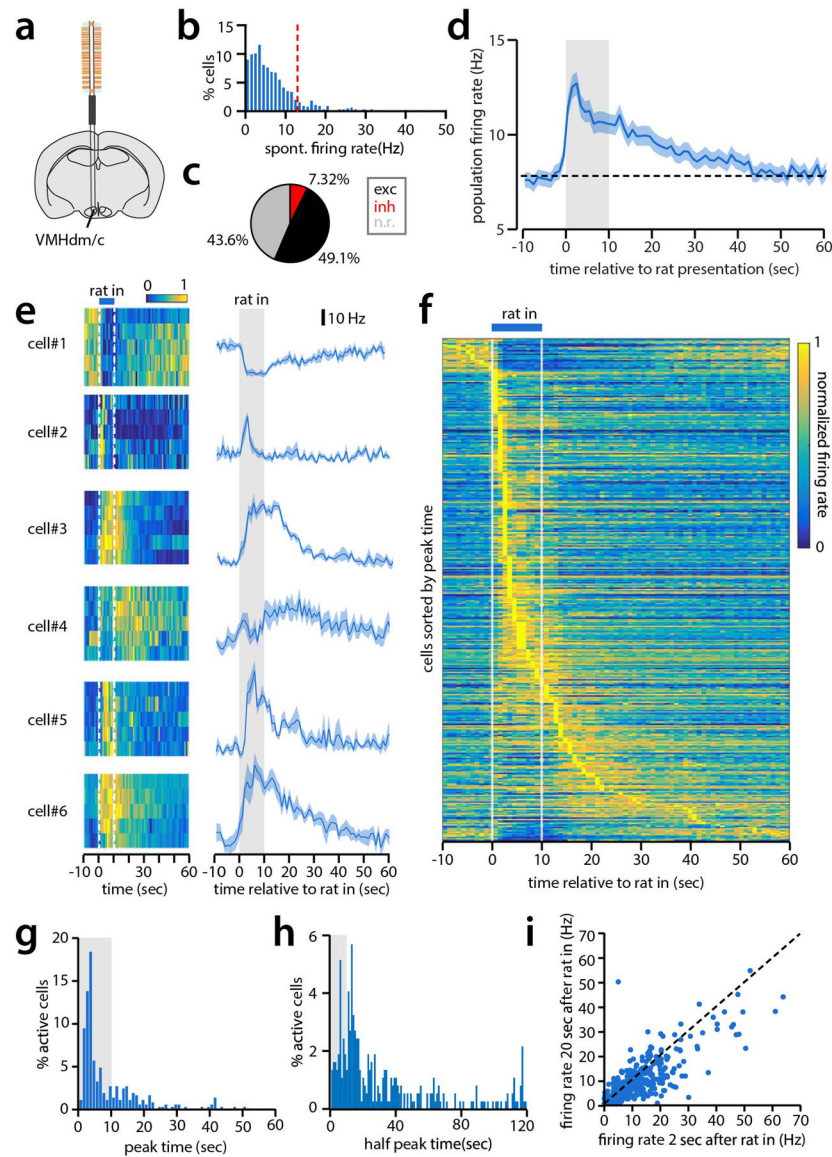
a. Schematic illustration of the experimental design used to transduce the majority of VMHdmSF1 neurons with Cre-dependent GCaMP7s and a minority of VMHdmSF1 neurons with Cre-dependent ChrimsonR-tdTomato, for the study of functional connectivity in VMHdm. **b.** Schematic illustration of the experimental design used to identify functional connectivity among VMHdmSF1 neurons using whole-cell patch-clamp recordings guided

by differential expression of GCaMP and ChrimsonR-tdTomato. **c**, Maximum projection confocal image of a VMHdmSF1 neuron recorded *ex vivo*, and filled with Neurobiotin conjugated to a far red fluorophore (AlexaFluor647; n = 7 neurons recorded and filled in 7 slices from 5 mice). **d**, Left – Average of voltage-clamp recordings at the reversal of inhibition ($V_{\text{Hold}} = -70$ mV) indicative of a post-synaptic response following photostimulation of ChrimsonR (blue line), sensitive to glutamate receptor blockage (black line; n=7 cells from 5 mice, 6/7 cells connected; mean \pm SEM). Middle – Quantification of the optically evoked excitatory post-synaptic current in control, *vs* glutamate receptor blockade conditions (n=7 cells per condition, two-tailed paired *t*-test, box plot elements for control condition; minimum = -31.10 pA, 25% percentile = -26.60 pA, median = -20.10 pA, 75% percentile = -11.80 pA, maximum = -0.1 pA, box plot elements for glutamate receptor blockade condition; minimum = -2.10 pA, 25% percentile = -0.90 pA, median = 0.20 pA, 75% percentile = 1.60 pA, maximum = 2.2 pA). Right – Frequency distribution of the optically evoked excitatory post-synaptic currents in a 15 millisecond window. **e**, *Ex vivo* single neuron whole-cell patch-clamp electrophysiology and Ca^{2+} imaging. Left column – Top, presentation of current-clamp recording during which a neuron from the field of view is clamped at -70 mV and depolarizing square pulses are delivered to induce action potential firing. Left column – Bottom, raster plot of Ca^{2+} imaging recordings identifying Ca^{2+} responsive cells following electrical stimulation of the patch-clamped neuron (highlighted by the magenta circle, neuron #90). Several other cells respond with an increase in their Ca^{2+} activity following electrical stimulation (highlighted by colored circles on the top right side of the activity color plot, neurons #87, #85, #82, #80, #78 and #66). Right – expanded view of the electrophysiology and superimposed imaging traces from four stimulation trials. **f**, Example cross-correlation color plot of the Ca^{2+} activity of the patch-clamped neuron (in this plot Cell #1), against the recorded Ca^{2+} activity of thirteen other VMHdmSF1 neurons. **g**, Quantification of follower cells per brain slice, identified as neurons with cross-correlation coefficient >0.6 compared *vs.* the Ca^{2+} trace of the electrically stimulated neuron (n = 5 brain slices from 5 mice, box plot elements; minimum = 2, 25% percentile = 2.5, median = 4, 75% percentile = 6.5, maximum = 8).



Extended Data 5. Summary of fiber/GRIN lens placements.

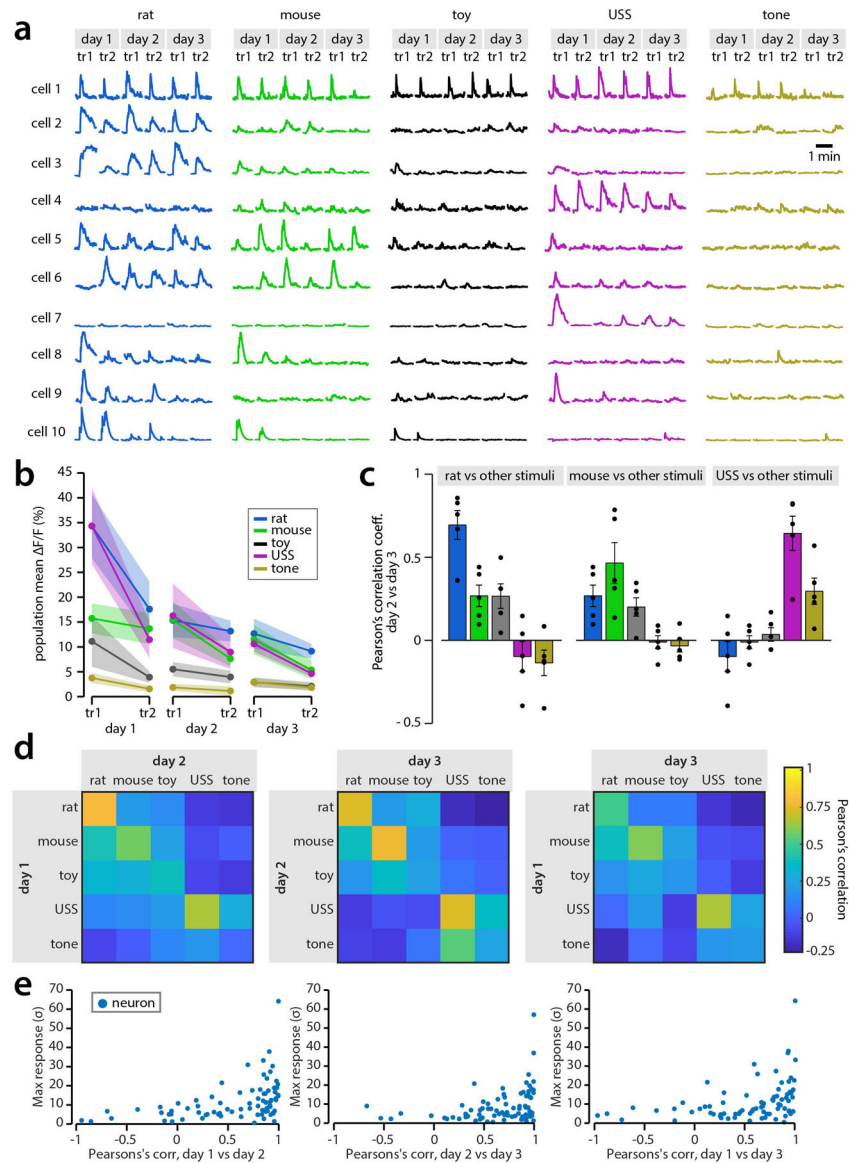
a, Map of the recording sites for fiber-photometry mice included in Figure 1. **b**, Map of the microscope GRIN lens location for mice illustrated in Figures 2–3. **c**, Map of the fiber tip locations in optogenetic silencing (iC++) mice illustrated in Figure 1. **d**, Map of the recording sites for tetanus toxin light chain (TTX) experiment mice illustrated in Figure 1. Anatomical images from⁴⁴.



Extended Data 6. Confirmation of VMHdm/c population dynamics using *in-vivo* electrophysiology.

a. Schematic illustrating silicon probe recording from VMHdm/c in head-fixed mouse. **b.** Histogram of the spontaneous firing rate of all recorded cells in VMHdm. Red dotted line indicates that 90% of cells have a spontaneous firing rate < 13 Hz. **c.** Percent of cells excited, inhibited, or not responsive to rat. A similar percentage of rat-responsive cells was detected by microendoscopic imaging of calcium activity (Figure 3I). **d.** Mean population firing rate evoked by rat. All firing rates in this figure were estimated in one-second time bins. ($n = 5$ mice, mean \pm SEM). **e.** Rat evoked responses in six example cells. Left, color map showing the normalized firing rate of individual cells on each of five repeated trials. White dotted lines mark the duration of rat presentation. Right, traces showing the average firing rate over the five trials (mean \pm SEM). **f.** Trial averaged, normalized firing rates of rat-responsive cells, sorted by time of response peak. **g.** Histogram of times to peak firing rate for rat responsive cells; compare to Figure 2k ($n = 370$ cells from 5 mice). **h.** Histogram of times of

decay to half of the peak firing rate for rat responsive cells, compare to Figure 2n (n same as in g). **i**, Scatter plot comparing cell responses at 2 or 20 seconds after rat introduction (n same as in g).

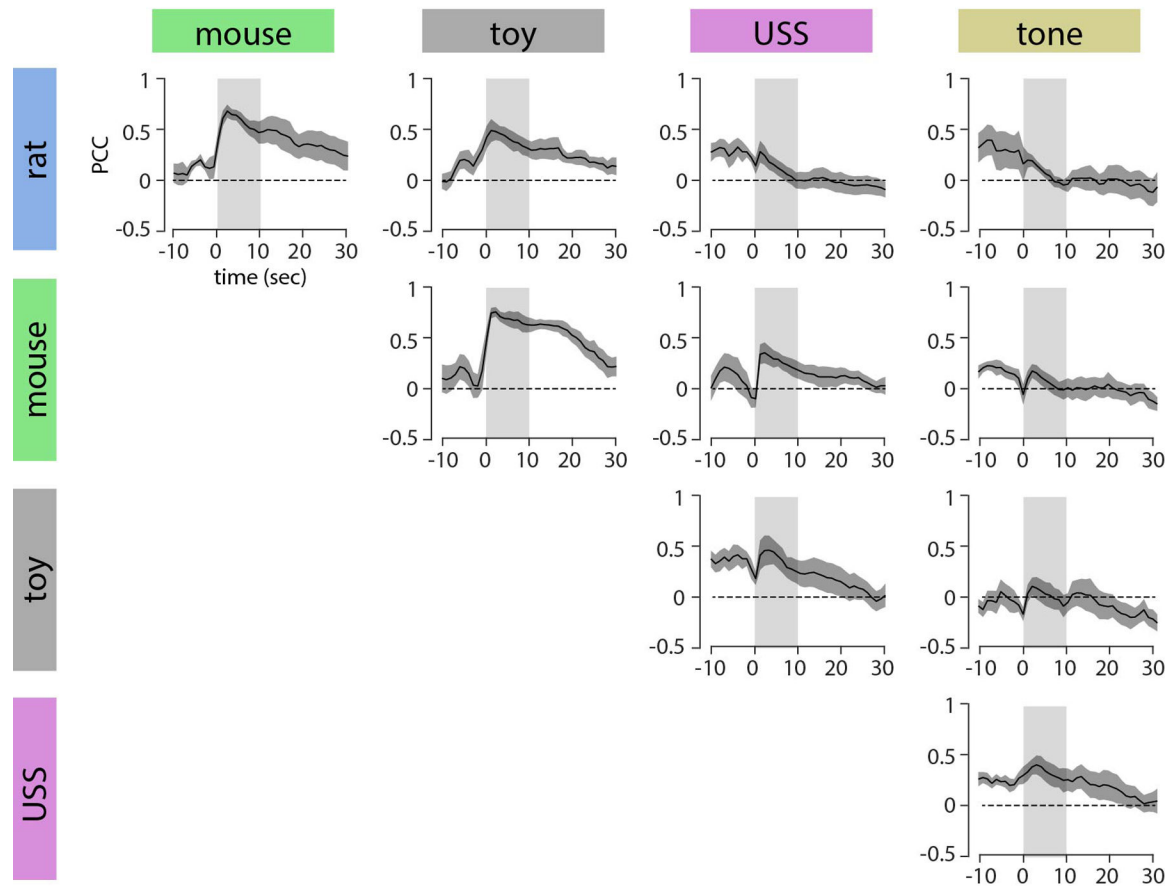


Extended Data 7. Stability of the VMHdm^{SF1} population response across trials and days.

a, Responses of ten example VMHdm^{SF1} neurons across three days of imaging, from the n=5 microendoscopic imaging mice. The five stimuli are presented for two trials (tr1, tr2) each day in pseudorandomized order, with ten minutes between stimulus presentations, on 3 consecutive days. Some cells show strong, consistent tuning across all trials/days (cells 1–4). Other neurons show consistent tuning, but have trial-to-trial variability in response sizes (cells 5–7). Others show adaptation of their responses across trials and days (cells 8–10). **b**, Population mean response to different stimuli on each trial across three days of imaging, showing a decrease in the population response across trials and days. (n=5 mice, mean

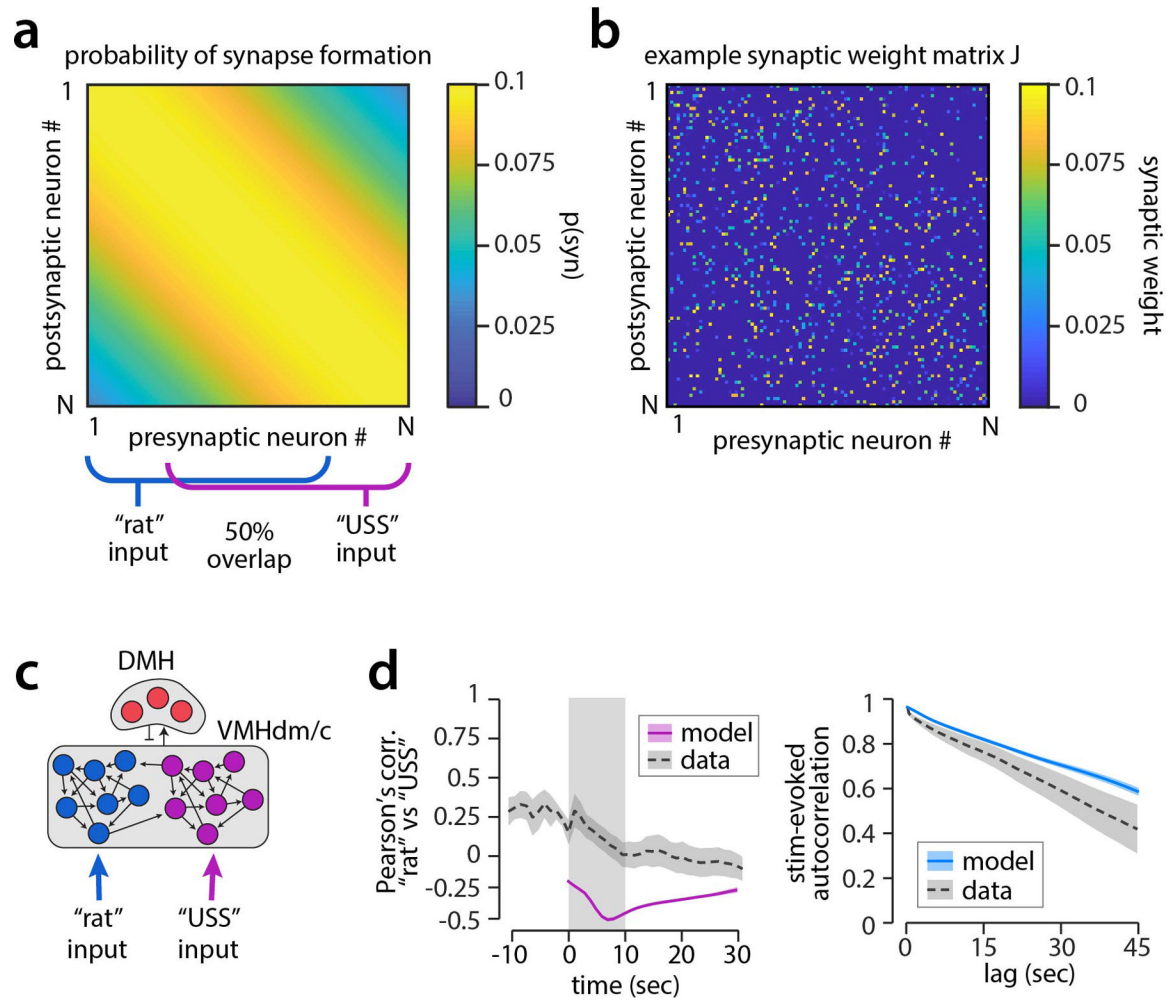
\pm SEM) **c**, Pearson's correlation between stimulus-evoked population activity on day 2 vs day 3 of imaging ($n=5$ mice, mean \pm SEM). While there is some trial-to-trial and day-to-day variability in cells' responses, stimulus identity is maintained by the population across days: this is reflected by the higher Pearson's correlation of a stimulus with itself than with other stimuli, and by the accuracy of decoders trained to predict stimulus identity from population activity (see Figure 3m–n, ED Figure 8). **d**, Matrix of Pearson's correlation between the mean population responses to all stimuli on day A and the responses on day B, for days 1 vs 2, days 2 vs 3, and days 1 vs 3 (mean across $n=5$ mice). **e**, Pearson's correlation between each cell's time-averaged response to all five stimuli on day A vs that cell's responses on day B, plotted against that cell's response to its most strongly preferred stimulus. Cells with small max responses (lower y-axis values) can show variability in their activity from day to day (reflected in a lower Pearson's correlation on the x-axis), while cells that show strong responses to one or more stimuli (higher y-axis values) tend to be more consistent in their stimulus tuning from day to day (higher PCC).

inter-stimulus Pearson's correlation coefficient (PCC)



Extended Data 8. Additional Pearson's correlations between stimulus pairs.

Pearson's correlation between VMHdm^{SF1} population activity as a function of time, evoked by all possible pairs of stimuli ($n=5$ imaged mice; mean \pm SEM).



Extended Data 10. Locally connected model networks.

a, Probability of synapse formation between neuron pairs decreases moderately as a function of “distance” (neuron number) in the locally connected sRNN model. Segments of the model targeted by rat and USS model input are also shown (blue/purple lines.) **b**, Example synaptic weight matrix generated from probability matrix shown in **a**; for visibility every 10th model neuron is shown. **c**, Example of a more highly structured model network, in which largely separate populations of neurons respond to the rat vs USS model inputs. **d**, Pearson’s correlation (left graph) and stimulus-evoked autocorrelation (right graph) for a network model such as that in **c**, in which network structure results in no overlap between rat and USS representations, whereas the actual data ($n=5$ mice; dashed black line with gray SEM envelope; data reproduced from Figure 4) shows partial overlap.

Supplementary Material

Refer to Web version on PubMed Central for supplementary material.

ACKNOWLEDGMENTS

We thank R. Palmiter for providing TetTox-GFP in advance of publication, H. Inagaki, M. Meister, L.F. Abbott, U. Rutishauser, and members of the Anderson lab for helpful comments on the manuscript, R. Remedios for help with miniscope imaging, L. Liu for teaching silicon probe recording, A. Vinograd for preliminary imaging experiments, T. Davidson and K. Deisseroth for teaching fiber photometry, B. Yang for helping with TetTox fiber photometry experiment, X. Da, J.S. Chang and C. Kim for technical assistance, X. Da and C. Chiu for laboratory management and G. Mancuso for administrative support. This work was supported by NIH Grant R01 MH112593. K99 MH117264 to A.K., a grant from the Simons Collaboration on the Global Brain Foundation (award #542947), a Helen Hay Whitney Foundation Postdoctoral Fellowship to L. L., and the EMBO ALTF 736-2018 to S.S. D.J.A. is an Investigator of the Howard Hughes Medical Institute.

WORKS CITED

1. Major G & Tank D Persistent neural activity: prevalence and mechanisms. *Current opinion in neurobiology* 14, 675–684, doi:10.1016/j.conb.2004.10.017 (2004). [PubMed: 15582368]
2. Curtis CE & Lee D Beyond working memory: the role of persistent activity in decision making. *Trends Cogn Sci* 14, 216–222, doi:10.1016/j.tics.2010.03.006 (2010). [PubMed: 20381406]
3. Anderson DJ & Adolphs R A framework for studying emotions across species. *Cell* 157, 187–200, doi:10.1016/j.cell.2014.03.003 (2014). [PubMed: 24679535]
4. Gross CT & Canteras NS The many paths to fear. *Nature reviews. Neuroscience* 13, 651–658, doi:10.1038/nrn3301 (2012). [PubMed: 22850830]
5. Kunwar PS et al. Ventromedial hypothalamic neurons control a defensive emotion state. *Elife* 4, doi:10.7554/eLife.06633 (2015).
6. Silva BA et al. Independent hypothalamic circuits for social and predator fear. *Nature neuroscience* 16, 1731–1733, doi:10.1038/nn.3573 (2013). [PubMed: 24212674]
7. Silva BA et al. The ventromedial hypothalamus mediates predator fear memory. *Eur J Neurosci* 43, 1431–1439, doi:10.1111/ejn.13239 (2016). [PubMed: 26991018]
8. Wang L, Chen IZ & Lin D Collateral Pathways from the Ventromedial Hypothalamus Mediate Defensive Behaviors. *Neuron*, doi:10.1016/j.neuron.2014.12.025 (2015).
9. Guo ZV et al. Maintenance of persistent activity in a frontal thalamocortical loop. *Nature* 545, 181–186, doi:10.1038/nature22324 (2017). [PubMed: 28467817]
10. Inagaki HK, Fontolan L, Romani S & Svoboda K Discrete attractor dynamics underlies persistent activity in the frontal cortex. *Nature* 566, 212–217, doi:10.1038/s41586-019-0919-7 (2019). [PubMed: 30728503]
11. Gunaydin LA et al. Natural neural projection dynamics underlying social behavior. *Cell* 157, 1535–1551, doi:10.1016/j.cell.2014.05.017 (2014). [PubMed: 24949967]
12. Papes F, Logan DW & Stowers L The vomeronasal organ mediates interspecies defensive behaviors through detection of protein pheromone homologs. *Cell* 141, 692–703, doi:10.1016/j.cell.2010.03.037 (2010). [PubMed: 20478258]
13. Yilmaz M & Meister M in *Current biology : CB Vol. 23 2011–2015* (Elsevier Ltd, 2013). [PubMed: 24120636]
14. Simon P, Dupris R & Costentin J Thigmotaxis as an index of anxiety in mice: influence of dopaminergic transmissions. *Behavioral brain research* 61, 59–64 (1994).
15. Berndt A et al. Structural foundations of optogenetics: Determinants of channelrhodopsin ion selectivity. *Proceedings of the National Academy of Sciences of the United States of America* 113, 822–829, doi:10.1073/pnas.1523341113 (2016). [PubMed: 26699459]
16. Han S, Soleiman MT, Soden ME, Zweifel LS & Palmiter RD Elucidating an Affective Pain Circuit that Creates a Threat Memory. *Cell* 162, 363–374, doi:10.1016/j.cell.2015.05.057 (2015). [PubMed: 26186190]
17. Dana H et al. Sensitive red protein calcium indicators for imaging neural activity. *Elife* 5, doi:10.7554/eLife.12727 (2016).
18. Ziv Y et al. Long-term dynamics of CA1 hippocampal place codes. *Nat Neurosci* 16, 264–266, doi:10.1038/nn.3329 (2013). [PubMed: 23396101]

19. Remedios R et al. Social behaviour shapes hypothalamic neural ensemble representations of conspecific sex. *Nature* 550, 388–392, doi:10.1038/nature23885 (2017). [PubMed: 29052632]
20. Ben-Shaul Y, Katz LC, Mooney R & Dulac C In vivo vomeronasal stimulation reveals sensory encoding of conspecific and allospecific cues by the mouse accessory olfactory bulb. *Proceedings of the National Academy of Sciences of the United States of America* 107, 5172–5177, doi:10.1073/pnas.0915147107 (2010). [PubMed: 20194746]
21. Mongeau R, Miller GA, Chiang E & Anderson DJ Neural correlates of competing fear behaviors evoked by an innately aversive stimulus. *J Neurosci* 23, 3855–3868 (2003). [PubMed: 12736356]
22. Arch VS & Narins PM “Silent” signals: Selective forces acting on ultrasonic communication systems in terrestrial vertebrates. *Anim Behav* 76, 1423–1428, doi:10.1016/j.anbehav.2008.05.012 (2008). [PubMed: 19802327]
23. McCormick DA Brain calculus: neural integration and persistent activity. *Nat Neurosci* 4, 113–114, doi:10.1038/83917 (2001). [PubMed: 11175863]
24. Goldman M, Compte A & Wang X-J Neural Integrators: recurrent mechanisms and models. *New Encyclopedia of Neuroscience*, 1–26 (2007).
25. Wang X-J Synaptic reverberation underlying mnemonic persistent activity. *Trends in Neuroscience* 24, 455–463 (2001).
26. Jan YN, Jan LY & Kuffler SW Further evidence for peptidergic transmission in sympathetic ganglia. *Proceedings of the National Academy of Sciences of the United States of America* 77, 5008–5012, doi:10.1073/pnas.77.8.5008 (1980). [PubMed: 6254052]
27. Wang XJ Synaptic basis of cortical persistent activity: the importance of NMDA receptors to working memory. *J Neurosci* 19, 9587–9603 (1999). [PubMed: 10531461]
28. Sompolinsky H, Crisanti A & Sommers H-J Chaos in random neural networks. *Physical review letters* 61, 259(1988). [PubMed: 10039285]
29. Toyozumi T & Abbott LF Beyond the edge of chaos: amplification and temporal integration by recurrent networks in the chaotic regime. *Phys. Rev. E* 84, 051908(051908), doi:10.1103/PhysRevE.84.051908 (2011).
30. Viskaitis P et al. Modulation of SF1 Neuron Activity Coordinately Regulates Both Feeding Behavior and Associated Emotional States. *Cell Rep* 21, 3559–3572, doi:10.1016/j.celrep.2017.11.089 (2017). [PubMed: 29262334]
31. Jan YN, Jan LY & Kuffler SW A peptide as a possible transmitter in sympathetic ganglia of the frog. *Proceedings of the National Academy of Sciences of the United States of America* 76, 1501–1505, doi:10.1073/pnas.76.3.1501 (1979). [PubMed: 35789]
32. Zelikowsky M et al. The Neuropeptide Tac2 Controls a Distributed Brain State Induced by Chronic Social Isolation Stress. *Cell* 173, 1265–1279 e1219, doi:10.1016/j.cell.2018.03.037 (2018). [PubMed: 29775595]
33. Kim D-W et al. Multimodal analysis of cell types in a hypothalamic node controlling social behavior. *Cell* 179, 713–728 (2019). [PubMed: 31626771]
34. Bellot-Saez A, Kekesi O, Morley JW & Buskila Y Astrocytic modulation of neuronal excitability through K(+) spatial buffering. *Neuroscience and biobehavioral reviews* 77, 87–97, doi:10.1016/j.neubiorev.2017.03.002 (2017). [PubMed: 28279812]
35. Motta SC et al. Dissecting the brain’s fear system reveals the hypothalamus is critical for responding in subordinate conspecific intruders. *Proceedings of the National Academy of Sciences of the United States of America* 106, 4870–4875, doi:10.1073/pnas.0900939106 (2009). [PubMed: 19273843]
36. Miller SM, Marcotulli D, Shen A & Zweifel LS Divergent medial amygdala projections regulate approach-avoidance conflict behavior. *Nat Neurosci* 22, 565–575, doi:10.1038/s41593-019-0337-z (2019). [PubMed: 30804529]
37. Dhillon H et al. Leptin directly activates SF1 neurons in the VMH, and this action by leptin is required for normal body-weight homeostasis. *Neuron* 49, 191–203, doi:S0896–6273(05)01134–7 [pii] 10.1016/j.neuron.2005.12.021 (2006). [PubMed: 16423694]
38. Xu X et al. Modular genetic control of sexually dimorphic behaviors. *Cell* 148, 596–607, doi:10.1016/j.cell.2011.12.018 (2012). [PubMed: 22304924]

39. Yang CF et al. Sexually dimorphic neurons in the ventromedial hypothalamus govern mating in both sexes and aggression in males. *Cell* 153, 896–909, doi:10.1016/j.cell.2013.04.017 (2013). [PubMed: 23663785]
40. Correa SM et al. An estrogen-responsive module in the ventromedial hypothalamus selectively drives sex-specific activity in females. *Cell Rep* 10, 62–74, doi:10.1016/j.celrep.2014.12.011 (2015). [PubMed: 25543145]
41. Ishii KK et al. A Labeled-Line Neural Circuit for Pheromone-Mediated Sexual Behaviors in Mice. *Neuron* 95, 123–137 e128, doi:10.1016/j.neuron.2017.05.038 (2017). [PubMed: 28648498]
42. Lerner TN et al. Intact-Brain Analyses Reveal Distinct Information Carried by SNc Dopamine Subcircuits. *Cell* 162, 635–647, doi:10.1016/j.cell.2015.07.014 (2015). [PubMed: 26232229]
43. Lu J et al. MINIPIPE: A Miniscope 1-Photon-Based Calcium Imaging Signal Extraction Pipeline. *Cell reports* 23, 3673–3684, doi:10.1016/j.celrep.2018.05.062 (2018). [PubMed: 29925007]
44. Franklin KBJ & Paxinos G THE MOUSE BRAIN IN STEREOTACTIC COORDINATES. Vol. Third edition (2008).
45. Yang L, Lee K, Villagracia J & Masmanidis SC Open source silicon microprobes for high throughput neural recording. *J Neural Eng* 17, 016036, doi:10.1088/1741-2552/ab581a (2020). [PubMed: 31731284]
46. Zhou P et al. Efficient and accurate extraction of in vivo calcium signals from microendoscopic video data. *Elife* 7, doi:10.7554/eLife.28728 (2018).
47. Giovannucci A et al. CalmAn an open source tool for scalable calcium imaging data analysis. *Elife* 8, doi:10.7554/eLife.38173 (2019).
48. Walz W Role of astrocytes in the clearance of excess extracellular potassium. *Neurochemistry international* 36, 291–300 (2000). [PubMed: 10732996]

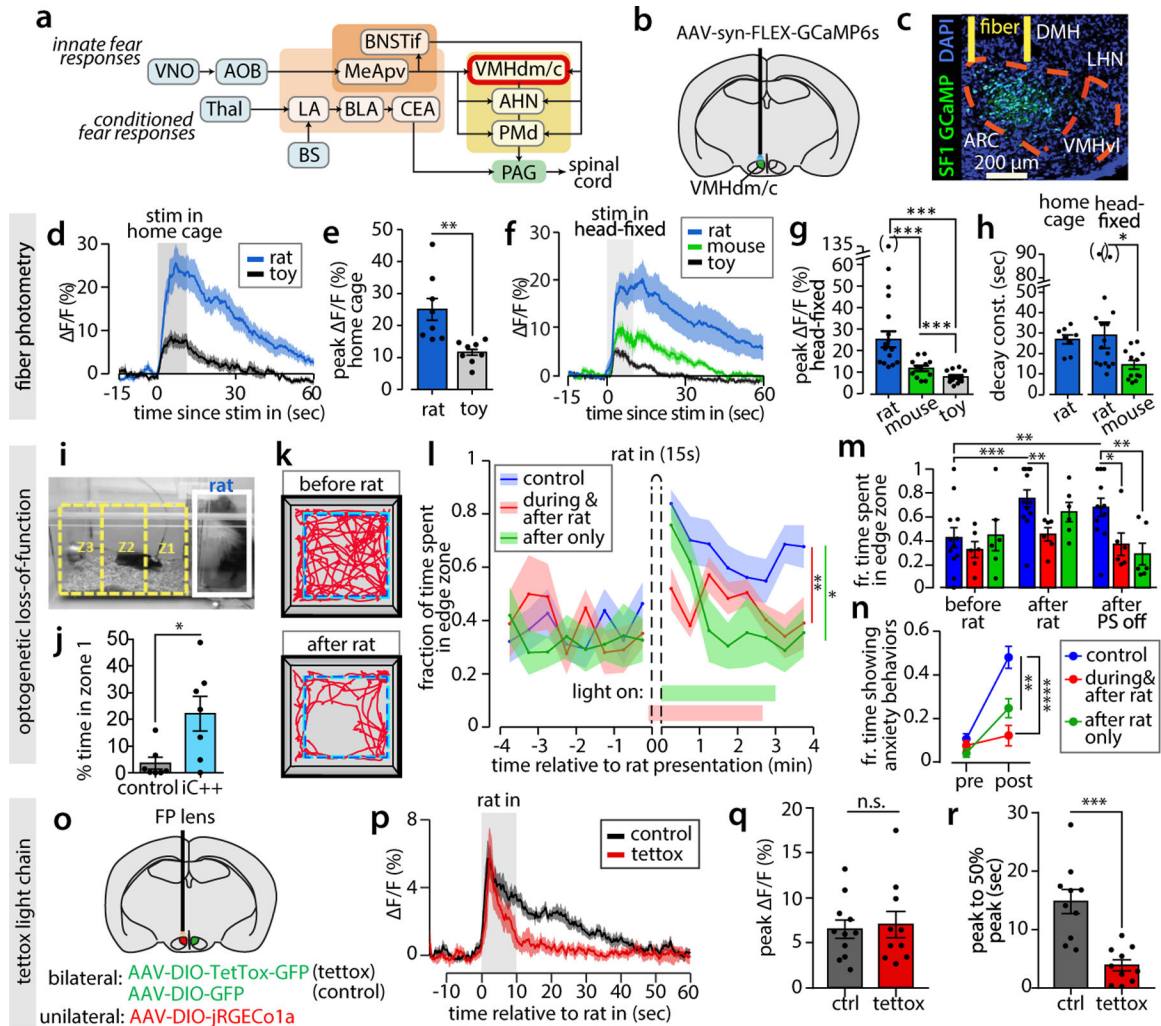


Figure 1. Persistent activity in VMHdm^{SF1} neurons evoked by predatory and conspecific cues. For all plots in all figures, ns = $p > 0.05$, * = $p < 0.05$, ** = $p < 0.01$, *** = $p < 0.001$, **** = $p < 0.0001$. Exact p-values and statistical tests used are reported in Supplementary Table 1. **a**, Circuits for innate and learned fear. Abbreviations in Methods. **b**, Site of fiber photometry in VMHdm/c (green). **c**, GCaMP6s expression in VMHdm^{SF1} neurons. **d**, Activity of VMHdm^{SF1} neurons in freely moving mice exposed to an anesthetized rat or toy rat for 10 seconds (gray shading). (n = 4 mice; mean ± SEM). **e**, Peak activity from (**d**) (n = 4 mice; mean ± SEM). **f**, Responses of VMHdm^{SF1} neurons in head-fixed mice to a cage holding an awake rat, mouse, or toy rat (n = 6 mice; mean ± SEM). **g**, Peak activity from (**f**) (n = 6 mice; mean ± SEM). **h**, Decay constants of activity in freely moving (“home cage”) or head fixed mice (home cage n = 4; head-fixed n = 6; mean ± SEM). (•) in **g**, **h** outlier data points that were omitted from significance testing. **i**, Home cage rat exposure assay. **j**, Percent time in zone 1 during 3-minute rat presentation (n = 7 Cre-dependent iC++ virus-injected SF1-Cre mice; n = 7 control Cre-dependent iC++ virus-injected wild-type littermates; mean ± SEM.). **k**, Tracking of mouse in open field rat exposure assay, blue line marks “edge zone”. **l**, Fraction of time spent in edge zone. Colored horizontal bars denote photostimulation (PS) periods (n = 12 control mice, n = 6 iC++ mice with PS during and after rat; n = 6 iC++ mice

with PS after rat only. Repeated measures ANOVA test. mean \pm SEM. For additional control EYFP virus-injected SF1-Cre mice, see ED Fig. 3j.) **m**, Mean time in edge zone, times defined in Methods (same mice as **l**, mean \pm SEM). **n**, Fraction (fr.) of time showing anxiety behaviors (see Methods) before (pre) vs after (post) rat exposure. (same mice as **l**, mean \pm SEM). **o**, Fiber photometry recording of VMHdm^{SF1} neurons in mice bilaterally expressing tetanus toxin light chain (or GFP control) and the red-shifted calcium indicator jRGEC01a. **p**, Activity of VMHdm^{SF1} neurons in head-fixed mice exposed to a live rat for ten seconds (gray shading). (n = 5 mice for both groups; mean \pm SEM.) **q**, Peak activity for data in (**p**) (“ctrl” = control; same mice as (**p**); mean \pm SEM). **r**, Decay time from peak to 50% peak for data in (**p**) (same mice as (**p**); mean \pm SEM).

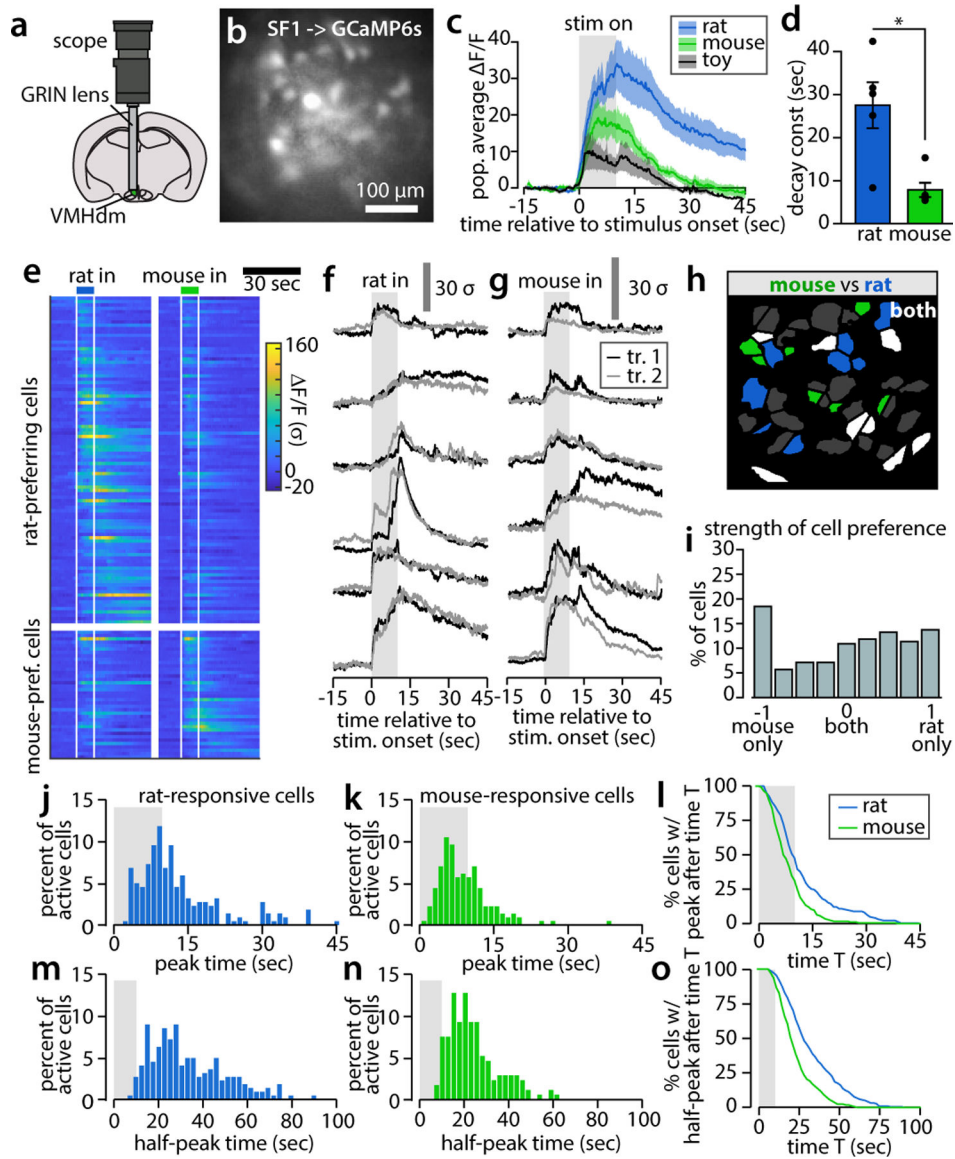


Figure 2. Microendoscopic imaging reveals persistence emerges from population activity.
a, Microendoscopic imaging in VMHdm/c. **b**, Field of view in an imaged mouse. **c**, Mean population response of imaged neurons to each stimulus ($n = 2$ trials/mouse from 5 mice, mean \pm SEM). **d**, Fit decay constants of down-sampled population responses to rat and mouse ($n=5$ mice, mean \pm SEM). **e**, Rat- and mouse-preferring neuron responses (from $n=5$ mice, mean over 2 trials). **f**, Example cells responding to rat in one imaged mouse on two repeated trials. **g**, Example cells responding to mouse on two repeated trials (same mouse as **f**). **h**, Example spatial map of cells responsive to rat, mouse, or both (white). **i**, Histogram of cell tuning preference for rat vs. mouse. Cells at ± 1 respond exclusively to rat or mouse, respectively; cells at 0 (“both”) respond equally to both stimuli ($n = 219$ cells from 5 mice across 3 days of imaging). **j**, Peak time histogram for rat-responsive cells ($n = 202$ rat-responsive cells from 5 mice across 3 days of imaging). **k**, Peak times for mouse-responsive cells ($n = 160$ mouse-responsive cells from 5 mice across 3 days of imaging). **l**, Fraction of

cells with peak after time T . \mathbf{m} , Half-peak times for rat-responsive cells (n same as \mathbf{j}). \mathbf{n} , Half-peak times for mouse-responsive cells (n same as \mathbf{k}). \mathbf{o} , Fraction of cells with half-peak later than time, legend as in \mathbf{l} .

Author Manuscript

Author Manuscript

Author Manuscript

Author Manuscript

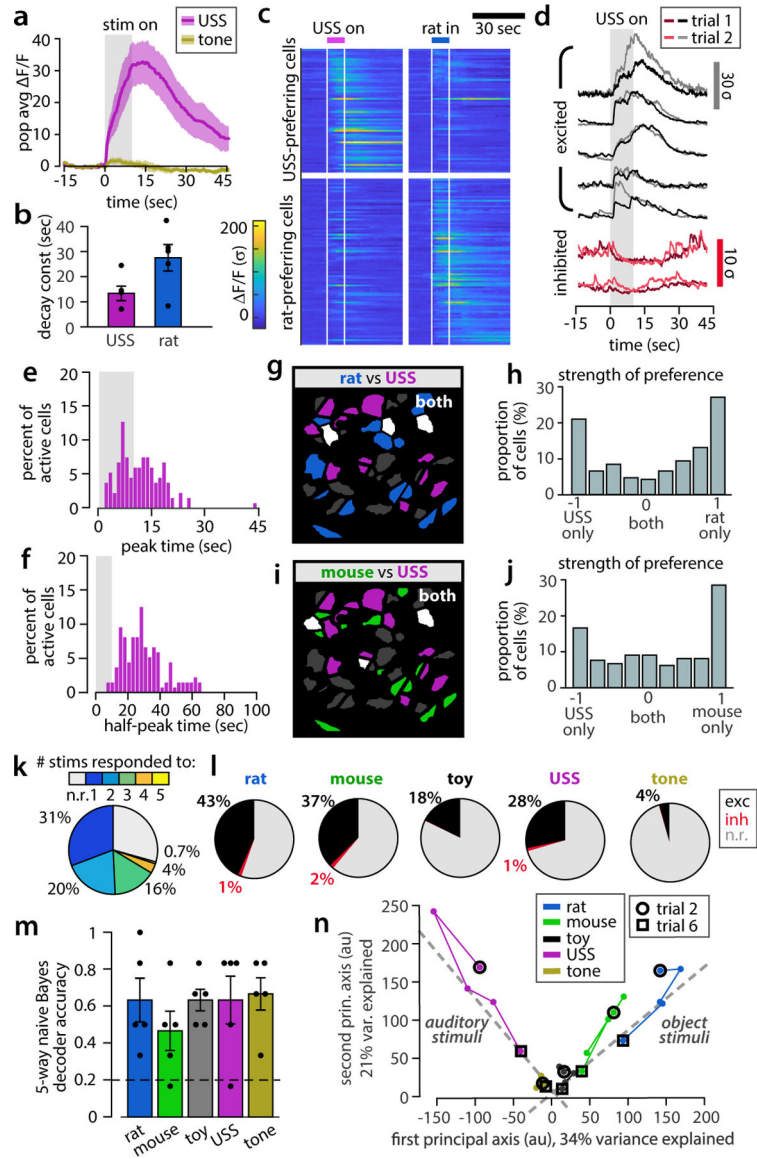


Figure 3. VMHdm^{SF1} neurons respond to a threatening auditory stimulus, and encode stimulus identity.

a, Mean VMHdm^{SF1} population response to aversive USS and 2 kHz tone ($n = 5$ mice, mean \pm SEM). **b**, Fit decay constants of population response to USS (rat reproduced from Fig 2d for comparison, mean \pm SEM). **c**, Rat- and USS-prefering neuron responses ($n=5$ mice, mean over 2 trials). **d**, Example cells responding to USS in one imaged mouse, on two repeated stimulus presentations. Black = excited cells, red = inhibited cells. **e**, Response peak times of USS-responsive cells ($n = 133$ USS-responsive cells from 5 mice across 3 days of imaging). **f**, Response half-peak times for USS-responsive cells (n same as **e**). **g**, Example spatial map of cells responsive to rat, USS, or both (white). **h**, Histogram of cell tuning preference, rat vs USS ($n = 216$ cells from 5 mice). **i**, Example spatial map of cells responsive to mouse and USS. **j**, Histogram of cell tuning preference, mouse vs USS ($n = 219$ cells from 5 mice). **k**, Percent of cells responding to zero (n.r.) to five out of five stimuli.

l, Percent of cells excited or inhibited by each stimulus. **m**, Accuracy of a 5-way decoder for stimulus identity from population activity (n=5 mice; mean \pm SEM). **n**, Principal component analysis (PCA) of time-averaged population responses, pooled across mice. Plotted points show 5 trials per stimulus, from 3 days of imaging.

Author Manuscript

Author Manuscript

Author Manuscript

Author Manuscript

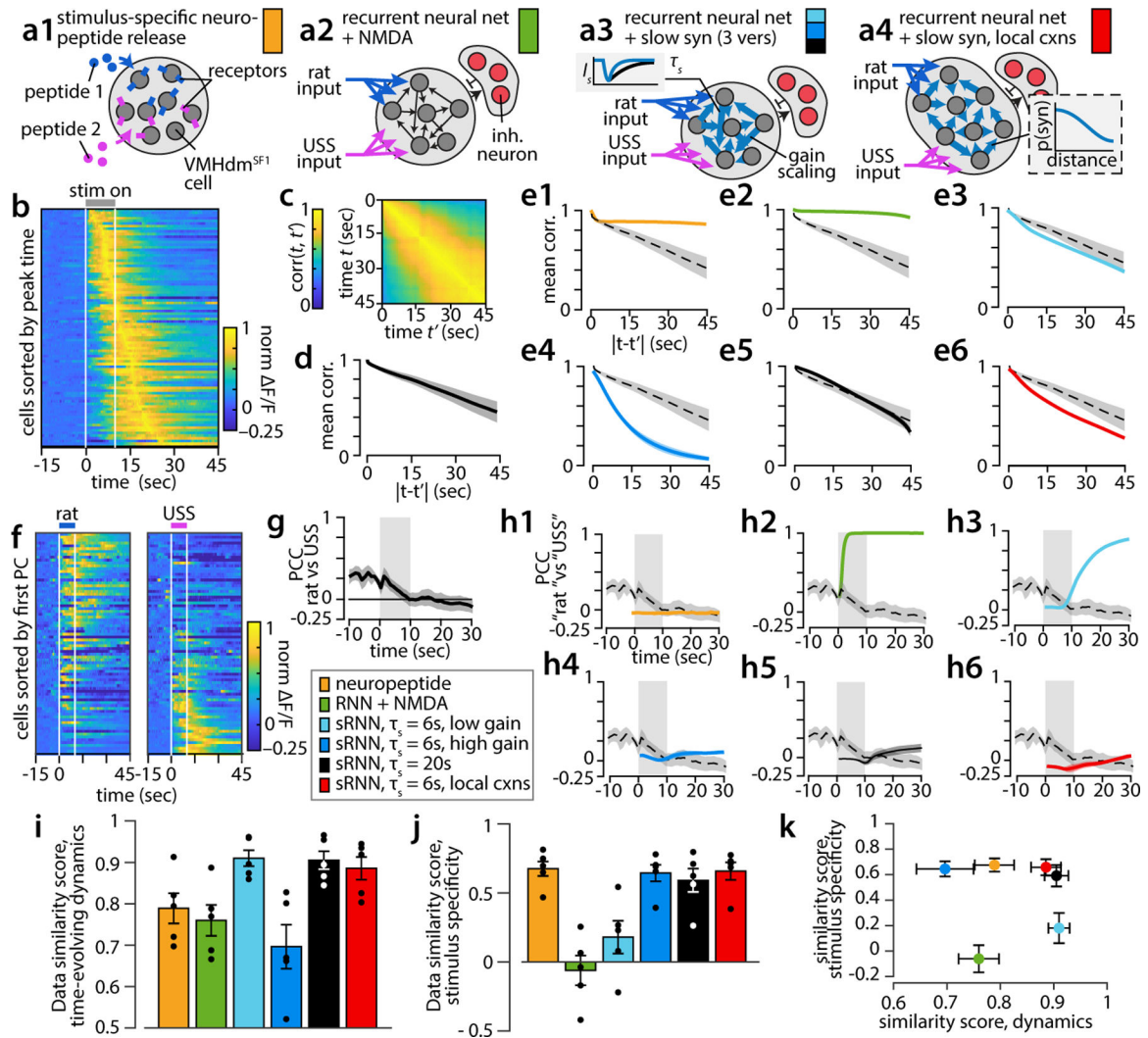


Figure 4. Data constrain set of computational models for persistent neural activity.

a. Six tested models of persistent activity. **a1**, slow-acting neuropeptide (or other neuromodulator) activation, no local connectivity between model neurons. **a2**, recurrent excitation in a randomly connected network with fast inhibitory feedback; persistence maintained via NMDA channels, time constant of NMDA excitation is $\tau_s = 200\text{ms}$. **a3** as in **a2**, but showing three versions with varying slower time constants of excitation (inset; light/dark blue, $\tau_s = 6\text{sec}$; black, $\tau_s = 20\text{sec}$), and different strengths of recurrent synapses (“gain scaling”, light/dark blue). **a4** as in **a3**, but with “local connections” (cxns) in which probability of a synapse $p(\text{syn})$ between neurons decreased with distance between cells (inset). **b**, Trial-averaged, normalized $\Delta F/F$ traces from USS-responsive neurons, sorted by time of response peak. **c**, Autocorrelation matrix of USS-evoked population activity. **d**, Time-averaged autocorrelation of USS-evoked population activity at different sampling intervals $|t-t'|$; ($n=5$ mice, mean \pm SEM). **e**, Autocorrelation as in **d**, for each model (colored lines; legend below panel **g**) compared to data (dashed line with gray SEM envelope; $n=10$ repeat simulations, mean \pm SEM). **f**, Trial-averaged $\Delta F/F$ traces from rat- or USS-responsive neurons, sorted by projection on first principal component. **g**, Pearson’s correlation between

rat- vs USS-evoked population activity as a function of time. **h**, Pearson's correlation between simulated "rat" and "USS" inputs to each model (colored lines), compared to data (dashed line with gray SEM envelope; n=10 repeat simulations, mean \pm SEM). **i**, "Similarity score" (see Methods) of models vs. data, summarizing plots in **e**. (n=5 mice, mean \pm SEM). **j**, Similarity score of model vs data, summarizing plots in **h**. (n=5 mice, mean \pm SEM). **k**, scatter plot of **i-j** (same mice as i-j; mean \pm SEM).